A pan-chromatic view of the galaxy cluster XMMU J1230.3+1339 at $z = 0.975^\star$

Observing the assembly of a massive system

R. Fassbender[1], H. Böhringer[1], J.S. Santos[2], G.W. Pratt[3], R. Šuhada[1], J. Kohnert[4], M. Lerchster[1,5], E. Rovilos[1], D. Pierini[1], G. Chon[1], A.D. Schwope[4], G. Lamer[4], M. Mühlegger[1], P. Rosati[6], H. Quintana[7], A. Nastasi[1], A. de Hoon[4], S. Seitz[5], and J.J. Mohr[1,5,8]

[1] Max-Planck-Institut für extraterrestrische Physik (MPE), Giessenbachstrasse 1, 85748 Garching, Germany
e-mail: `rfassben@mpe.mpg.de`
[2] INAF-Osservatorio Astronomico di Trieste, Via Tiepolo 11, 34131 Trieste, Italy
[3] CEA Saclay, Service d'Astrophysique, L'Orme des Merisiers, Bât. 709, 91191 Gif-sur-Yvette Cedex, France
[4] Astrophysikalisches Institut Potsdam (AIP), An der Sternwarte 16, 14482 Potsdam, Germany
[5] University Observatory Munich, Ludwigs-Maximillians University Munich, Scheinerstr. 1, 81679 Munich, Germany
[6] European Southern Observatory (ESO), Karl-Scharzschild-Str. 2, 85748 Garching, Germany
[7] Departamento de Astronomía y Astrofísica, Pontificia Universidad Católica de Chile, Casilla 306, Santiago 22, Chile
[8] Excellence Cluster Universe, Boltzmannstr. 2, 85748 Garching, Germany

ABSTRACT

Context. Observations of the formation and evolution of massive galaxy clusters and their matter components provide crucial constraints on cosmic structure formation, the thermal history of the intracluster medium (ICM), galaxy evolution, transformation processes, and gravitational and hydrodynamic interaction physics of the subcomponents.
Aims. We characterize the global multi-wavelength properties of the X-ray selected galaxy cluster XMMU J1230.3+1339 at $z = 0.975$, a new system discovered within the XMM-*Newton* Distant Cluster Project (XDCP). We measure and compare various widely used mass proxies and identify multiple cluster-associated components from the inner core region out to the large-scale structure environment.
Methods. We present a comprehensive galaxy cluster study based on a joint analysis of X-ray data, optical imaging and spectroscopy observations, weak lensing results, and radio properties for achieving a detailed multi-component view on a system at $z \sim 1$.
Results. We find an optically very rich and massive system with $M_{200} \simeq (4.2 \pm 0.8) \times 10^{14}\,M_\odot$, $T_{X,2500} \simeq 5.3^{+0.7}_{-0.6}\,\mathrm{keV}$, and $L^{\mathrm{bol}}_{X,500} \simeq (6.5 \pm 0.7) \times 10^{44}\,\mathrm{erg\,s^{-1}}$. We have identified a central fly-through group close to core passage and find marginally extended 1.4 GHz radio emission possibly associated with the turbulent wake region of the merging event. On the cluster outskirts we see evidence for an on-axis infalling group with a second Brightest Cluster Galaxy (BCG) and indications for an additional off-axis group accretion event. We trace two galaxy filaments beyond the nominal cluster radius and provide a tentative reconstruction of the 3D-accretion geometry of the system.
Conclusions. In terms of total mass, ICM structure, optical richness, and the presence of two dominant BCG-type galaxies, the newly confirmed cluster XMMU J1230.3+1339 is likely the progenitor of a system very similar to the local Coma cluster, differing by 7.6 Gyr of structure evolution. This new system is an ideally suited astrophysical model laboratory for in-depth follow-up studies on the aggregation of baryons in the cold and hot phases.

Key words. galaxies: clusters: general – galaxies: clusters: individual: XMMU J1230.3+1339 – X-rays: galaxies: clusters – galaxies:ellipticals and lenticular – galaxies: evolution – cosmology: dark matter – cosmology: observations

1. Introduction

Massive galaxy clusters at high redshift are unique laboratories to study galaxy evolution in the densest environments, the thermodynamic properties and chemical enrichment of the hot intra cluster medium (ICM) at large look-back times, and the structure and growth of the underlying virialized Dark Matter (DM) halos. Moreover, distant galaxy clusters are among the most promising cosmological probes to shed new light on the properties and

evolution of Dark Energy (DE). This potential has recently been demonstrated based on moderate size X-ray cluster samples out to redshift unity (e.g. Vikhlinin et al. 2009b; Allen et al. 2008) and is reflected in the armada of ongoing or planned galaxy cluster surveys in various wavelength regimes.

Progresses in observational capabilities and search techniques over the past five years have led to an increase in the number of spectroscopically confirmed $z \gtrsim 1$ clusters from a handful of objects to now a few dozen systems. On the X-ray side, new identifications of X-ray luminous clusters are currently largely driven by XMM-*Newton* serendipitous surveys (e.g. Mullis et al. 2005; Stanford et al. 2006; Fassbender et al. 2008; Santos et al. 2009; Schwope et al. 2010) and smaller dedicated surveys of a

---

few square degrees (e.g. Andreon et al. 2005; Bremer et al. 2006; Pierre et al. 2006; Finoguenov et al. 2007, 2010; Tanaka et al. 2010). Optical search methods based on overdensities of galaxies at similar color (e.g. Gladders & Yee 2005) have recently been successfully extended to the near-infrared (NIR) regime (e.g. van Breukelen et al. 2006), and the mid-infrared (MIR) with *Spitzer* (e.g. Stanford et al. 2005; Eisenhardt et al. 2008; Wilson et al. 2009; Muzzin et al. 2009; Demarco et al. 2010). The first detections of galaxy clusters based on the Sunyaev-Zeldovich effect (SZE) (Staniszewski et al. 2009; Vanderlinde et al. 2010) have opened another promising window for the selection and study of massive distant systems.

A crucial pre-requisite for linking galaxy cluster survey results to cosmological model predictions is reliable and well quantified mass-observable relations. In this respect, weak gravitational lensing techniques have emerged as a promising tool to achieve a robust calibration of various scaling relations. In the low redshift Universe, weak lensing (WL) based mass measurements applied to sizable cluster samples have established mass-observable relations with significantly improved accuracy (e.g. Reyes et al. 2008; Zhang et al. 2008; Marrone et al. 2009). First weak lensing constraints on the evolution of scaling relations for X-ray groups are now available (e.g. Leauthaud et al. 2010), and significant WL signals have been reported for individual massive clusters out to $z \sim 1.4$ (e.g. Jee et al. 2006, 2009). However, all mass estimation methods are potentially influenced by different inherent biases (e.g. Meneghetti et al. 2010) emphasizing the importance of an inter comparison of different techniques, in particular for high redshift systems.

Significant progress is yet to be made to establish robust mass-observable relations at $z \sim 1$ and beyond and to compare vices and virtues of mass proxies derived from optical/IR, X-ray, WL, and SZE observations at these redshifts. The current limitation is the still persisting small number of known galaxy clusters at $z > 0.9$ that are sufficiently massive to enable the detection and cross-comparison of all observational techniques on an individual cluster basis. Using concordance model parameters, we can estimate the surface density of suitable test objects at $z > 0.9$ with $M_{200} \gtrsim 4 \times 10^{14}\,M_{\odot}$ to be about one object in a solid angle of $100\,\mathrm{deg}^2$ (see e.g. Jee et al. 2009).

In this paper we present first details of the newly identified cluster of galaxies XMMU J1230.3+1339 at redshift $z = 0.975$. We perform a cluster characterization based on a joint analysis in X-rays, optical imaging and spectroscopy, and weak lensing. The three main science objectives of this work are (i) a multi-wavelength characterization of the physical system parameters, (ii) the derivation and cross-comparison of a dozen different total mass proxies, and (iii) the identification of substructure- and large-scale structure components for an assessment of the dynamical state of the system. An accompanying paper by Lerchster et al. (2010, Paper II hereafter) provides a more detailed view on the cluster's galaxy population and the performed weak lensing analysis.

The cluster XMMU J1230.3+1339 occupies a special noteworthy location in the sky, as it is located behind our closest neighbor, the Virgo system. The cluster center is in the direct proximity of the Virgo member NGC 4477, about 1.3 deg North of M87, corresponding to a projected distance of approximately $400\,\mathrm{kpc}$, or half of R_{500}, at the Virgo redshift.

This paper is organized as follows: Sect. 2 introduces the observations, data reduction, and first basic cluster properties; Sect. 3 contains the derived results and mass proxies; Sect. 4 focusses on a global pan-chromatic view and the identification of cluster associated sub-components; Sect. 5 discusses the dy-

namical state of the cluster and the comparison of mass proxies; we conclude in Sect. 6. Throughout the paper we assume a ΛCDM cosmology with $\Omega_{\mathrm{m}} = 0.3$, $\Omega_{\Lambda} = 0.7$, and $h = H_0/(100\,\mathrm{km\,s^{-1}\,Mpc^{-1}}) = 0.7$. Unless otherwise noted, the notation with subscript X_{500} (X_{200}) refers to a physical quantity X measured inside a radius, for which the mean total density of the cluster is 500 (200) times the critical energy density of the Universe $\rho_{\mathrm{cr}}(z)$ at the given redshift z. All reported magnitudes are given in the AB system. At redshift $z = 0.975$ the lookback time is 7.61 Gyr, one arcsecond angular distance corresponds to a projected physical scale of 7.96 kpc, and the cosmic evolution factor has a value of $E(z) = H(z)/H_0 = [\Omega_m(1 + z)^3 + \Omega_{\Lambda}]^{1/2} = 1.735$.

2. Observations, data reduction, and basic cluster properties

The cluster of galaxies XMMU J1230.3+1339 (see Fig. 1) was discovered as part of the XMM-*Newton* Distant Cluster Project (XDCP), a serendipitous archival X-ray survey focussed on the identification of very distant X-ray luminous systems (Mullis et al. 2005; Böhringer et al. 2005; Fassbender 2007). The first step of the survey strategy is based on the initial detection of serendipitous extended X-ray sources as cluster candidates in high galactic latitude XMM-*Newton* archival fields. Extended X-ray sources lacking an optical cluster counterpart in Digitized Sky Survey (DSS) images are followed-up as distant candidates by optical two-band imaging with the objective to confirm a galaxy overdensity and obtain a redshift estimate based on the color of early-type cluster galaxies. Subsequent spectroscopic observations of photometrically identified systems provide the final secure cluster identification as bound objects and accurate redshifts for the high-z systems. The presented XMM-*Newton* and the VLT/FORS 2 imaging and spectroscopy data are part of this XDCP survey data set.

Additional follow-up data for a more detailed characterization of the cluster were obtained with the Large Binocular Telescope (LBT) for deep multi-band imaging . Moreover, high-resolution X-ray data of a field serendipitously covering the cluster has recently become available in the *Chandra* archive. An overview of the full multi-wavelength data set used for this work is given in Table 2. We first present the optical imaging and spectroscopy data and then discuss the analysis of the archival X-ray data.

2.1. Optical follow-up observations

2.1.1. VLT Imaging

Short-exposure images in the R_{special} (960 s, hereafter R) and z_{Gunn} (480 s, hereafter z) filters were acquired in March 2007 with VLT/FORS 2 in photometric, sub-arcsecond seeing conditions in order to identify the optical counterpart associated with the extended X-ray source XMMU J1230.3+1339. The FORS 2 imaging data with a field-of-view of $6.8' \times 6.8'$ were reduced in a standard manner following the procedure described in Erben et al. (2005). The 4 (3) bias subtracted and flat-fielded frames in the z (R) band were registered to a common coordinate system and co-added using *SWarp* and *ScAMP* (Bertin 2006). The final stacked images have a measured on-frame seeing of $0.52''$ in the z-band and $0.62''$ in R.

Photometric zero-points were derived from dedicated standard star observations in the R-band and stellar SDSS photometry in the science field for the z filter. Photometric catalogs were
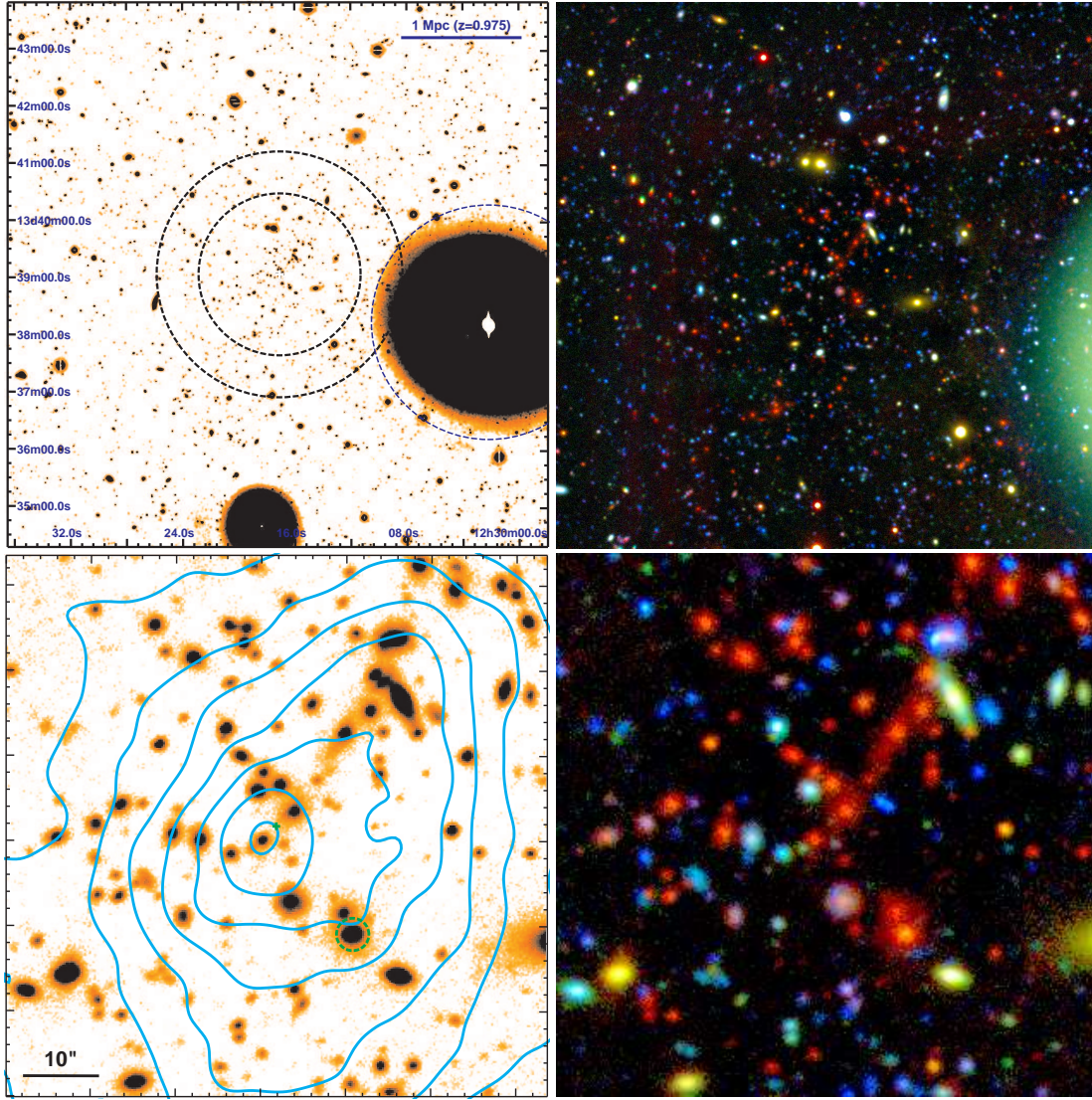
Fig. 1. Optical appearance of the galaxy cluster XMMU J1230.3+1339 at $z = 0.975$. *Top left:* Co-added $9.5' \times 9.5'$ i′z′ image showing the cluster environment. The dashed circles represent the projected cluster radii R_{200} (outer) and R_{500} (inner), the physical angular scale at the cluster redshift is given in the upper right corner, and the Virgo galaxy NGC 4477 is marked by the dashed circle on the right. *Top right:* RGB color composite based on the co-added LBT images in i′z′ (red channel), Vr′ (green), and UB (blue). The side length of the image corresponds to a physical scale of $2\,\mathrm{Mpc} \times 2\,\mathrm{Mpc}$ ($250'' \times 250''$), displaying approximately the region inside R_{200}. The large number of red cluster galaxies are easily visible. *Bottom left:* Core region of the cluster in i′z′ with *Chandra* X-ray contours overlaid in cyan and a side length of 560 kpc (70″); the green dashed circle marks the BCG to the South-West of the nominal X-ray center (green cross). *Bottom right:* Same sky region as on the left as color composite.

Table 1. Observation log of the X-ray, optical imaging, and spectroscopic data coverage of XMMU J1230.3+1339.

Observatory	Instrument	Data Type	Date	Exposure Time	Observation ID
XMM-*Newton*	EPIC	X-ray	Jun 2002	14 ksec / 3.9 h	0112552101
XMM-*Newton*	EPIC	X-ray	Jul 2002	13 ksec / 3.6 h	0106060401
Chandra	ACIS-S	X-ray	Apr 2008	38 ksec / 10.6 h	9527
VLT	FORS 2	R z imaging	11 Mar 2007	1.4 ksec / 0.4 h	078.A-0265
LBT	LBC	U B V r′ i′ z′ imaging	28 Feb - 2 Mar 2009	37 ksec / 10.3 h	
VLT	FORS 2	MXU spectroscopy	27 Apr & 6-7 Jun 2008	2.2 ksec / 3.9 h	081.A-0312

extracted from the PSF matched images using *SExtractor* (Bertin & Arnouts 1996) in dual image mode with the unconvolved z-band frame as detection image. The 50% completeness limits[1] for the two bands were estimated to be $z_{\mathrm{lim}}(50\%) \simeq 24.7$ mag and $R_{\mathrm{lim}}(50\%) \simeq 25.4$ mag.

For this work we limit the quantitative galaxy color assessment in the cluster environment to this initial FORS 2 R- and z-band discovery data set. We constructed the color-magnitude-diagram (CMD) for the observed field using the total (`MAG_AUTO`) z-band magnitude and fixed 2.2″ (3.5× seeing) aperture magnitudes for the R−z color, both corrected for effects of galactic extinction. The resulting CMD is displayed in Fig. 2 after the

removal of stellar sources (`CL_STAR`≥0.95) and objects with saturated cores. The richly populated cluster red-sequence, i.e. the locus of early-type cluster galaxies in the CMD, clearly stands out from the background at a color of R−z∼2 and provided an early indication that the galaxy cluster is indeed at $z > 0.9$ prompting the subsequent spectroscopic follow-up.

We have not attempted to fit a non-zero slope to the cluster red-sequence, since (i) the slope is expected to be small, (ii) the moderately deep ground-based data does not allow precision photometry down to faint magnitudes, and (iii) the lack of secure cluster membership and SED-type information along the ridgeline would bias the result due to possible inclusions of interlopers and non-passive galaxies. For a robust color selection of predominantly cluster galaxies with a high contrast with re-

---

[1] The 50% completeness corresponds approximately to a $5\,\sigma$ detection limit (2″ apertures).

spect to foreground and background objects we apply a simple color-cut of ± 0.2 mag (dotted lines in Fig. 2) around the median bright-end color of R−z∼2.05 (red dashed line). This color cut encompasses 11 out of 13 spectroscopically confirmed cluster members and should hence be a good approximation for the underlying physical red-sequence of the early-type cluster members, which is expected to be slightly bluer at the faint end driven mainly by a decreasing average metallicity with increasing apparent magnitude (e.g. Kodama & Arimoto 1997).

The lower panel of Fig. 2 shows the histogram of the number of objects along this color-selected strip $1.85 \leq R-z \leq 2.25$ mag in bins of 0.4 mag for galaxies within $1'$ of the X-ray center (blue solid line) and galaxies further away (black dotted line), with the nominal 50 % completeness limit at this color indicated by the red vertical line. The apparent decline of the number of red ridgeline galaxies towards fainter magnitudes seen in the blue histogram can be attributed to several possible factors, or combinations of these: (i) the increasing uncertainty for fainter galaxies in the R−z color determination scatters a fraction of red cluster galaxies outside the color cut, (ii) fainter ridgeline galaxies are preferentially located beyond a cluster-centric distance of $1'$ (dotted histogram), or (iii) the cluster red-sequence exhibits a physical deficit of faint galaxies as has been reported for several high-z clusters (e.g. De Lucia et al. 2007; Tanaka et al. 2007).

Figure 3 displays the cumulative radial distribution of red galaxies with the same color cuts as a function of cluster-centric distance (blue solid line). About 20 red galaxies are found beyond a cluster-centric distance of $1'$ but still within the fiducial cluster radius (solid vertical line, see Sect. 3.1.1). These galaxies can mostly be attributed to infalling groups, as discussed in Sect. 4.2.2, and could contribute to the faint end of the red population. The blue dotted line shows the average surface density of red galaxies within the cluster-centric distance r, which is directly related to the galaxy contrast in the enclosed area with respect to the background. This contrast can be optimized for the initial confirmation of the cluster and the identification of its red-sequence by restricting the galaxy selection to the inner $30''$ or $1'$ (vertical dashed lines), as was used for the CMD of Fig. 2.

For this work, only the particularly richly populated bright end of the red ridgeline in XMMU J1230.3+1339 is highlighted (for comparison see e.g. Mei et al. 2009). A more quantitative analysis of the physical cluster red-sequence (and a possible truncation thereof) based in the deeper LBT imaging data is discussed in Paper II.

2.1.2. LBT Imaging

In order to obtain a more detailed view of the cluster, we initiated deep wide-field imaging observations in six-bands U B V r' i' z'[2] with the Large Binocular Cameras (LBC) working in parallel at the 2×8.4 m Large Binocular Telescope. The data were acquired between 28 February and 2 March 2009 under good, mostly sub-arcsecond, seeing conditions. The net exposure times (per single 8.4 m telescope) over the field-of-view of $26' \times 26'$ were 9 ksec in the U and z'-bands, 5.9 ksec in B and i', 3.6 ksec in V, and 3.2 ksec in the r'-band.

The LBT/LBC imaging data were reduced in standard manner similar to the treatment in the previous section. For more information on LBC specific reduction procedures in general we refer to Rovilos et al. (2009), and for details on the photometric calibration and object catalogues based on this data set to Paper II. The reduced final co-added image stacks have measured seeing full-width half-maxima (FWHM) of $0.8''$ in the z'-band and about $0.9''$ in all other bands, resulting in limiting magnitudes (5σ detection in $1''$ apertures, see Table 1 of Paper II) of the co-added frames of: $U_{lim} \simeq 27.0$, $B_{lim} \simeq 26.9$, $V_{lim} \simeq 26.3$, $r'_{lim} \simeq 26.2$, $i'_{lim} \simeq 25.8$, and $z'_{lim} \simeq 25.4$.

This rich imaging data set will be fully exploited in forthcoming papers (e.g. Paper II). The current work uses the deep wide-field LBT imaging data for two main purposes: (i) a quantitative photometric analysis in the z'-band (Sect. 3.2), which is deeper than the FORS 2 data and allows accurate background determinations in independent external regions; and (ii) a deep optical view in single-band and color composites as shown in Figs. 1, 10, 11, and 13. In order to maximize the depth of the available data for visualization purposes, we co-added the i' and z'-band using an inverse variance weighting scheme to a resulting combined i'z'-frame. This combined band is used as single-band background image with a high contrast of cluster galaxies and as input for the red-channel of RGB color composite images. Accordingly, a co-added Vr'-frame was obtained as input for the green-channel, and a UB-image for the blue-channel.
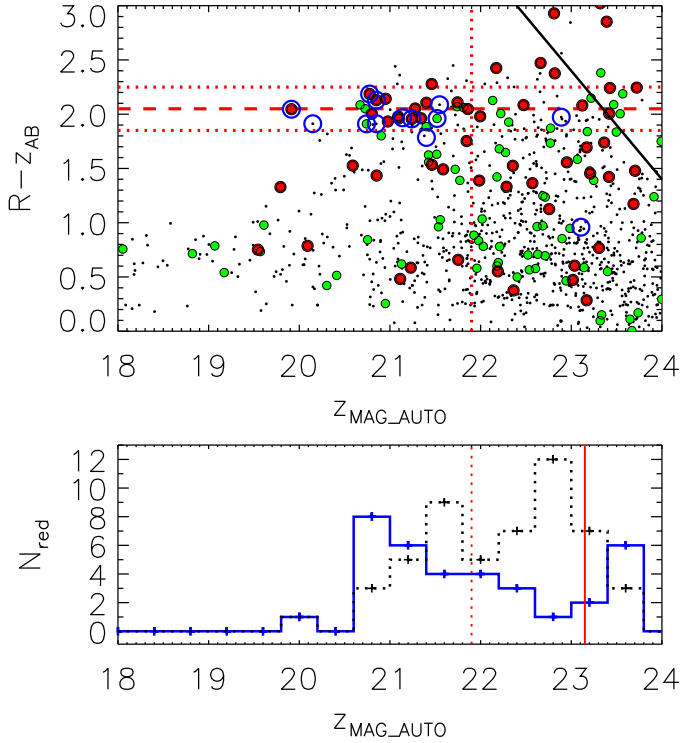
2.1.3. VLT Spectroscopy

For the final redshift determination of the cluster, we obtained spectroscopic observations with VLT/FORS 2 using a single MXU-mode (Mask eXchange Unit) slit-mask centered on XMMU J1230.3+1339 for a total net exposure time of 7.85 ksec (Table 1). Targeted galaxies were selected to be preferentially red galaxies close to the ridgeline in Fig 2. The chosen instrument setup with the 300 I grism and a slit width of $1''$ provides a wavelength coverage of 6000–10000 Å with a resolution of $R = 660$. The data consisted of six individual exposures taken in three different nights under variable seeing conditions ranging from $0.7''$ to $1.9''$.

The spectra were reduced with standard techniques using *IRAF*[3] tasks. In short, the 2-D spectra were bias subtracted, flat-fielded to correct for pixel-to-pixel variations, and co-added to provide a sufficient signal-to-noise ratio (SNR) for the tracing of weak spectra. 38 1-D spectra were extracted and sky-subtracted by fitting a low order polynomial to adjacent background regions along the trace of the spectrum. The wavelength calibration was achieved by means of a Helium-Argon reference line spectrum observed through the same MXU mask. The quality of the obtained dispersion solutions was cross-checked by measuring the observed position of several prominent sky lines yielding typical absolute rms calibration errors below 1 Å.

For the redshift determination, the reduced and wavelength calibrated spectra were cross-correlated with a range of galaxy template spectra using the *IRAF* package *RVSAO* (Kurtz & Mink 1998). Out of 38 spectra, we could identify 13 secure cluster members (see Table 2) with a median cluster redshift of $\bar{z} = 0.9745 \pm 0.0020$ and a bootstrapped error estimate. Figure 4 displays five sample spectra of cluster members with the most prominent spectral features labelled. The cross-correlation of absorption-line spectra with a sufficient signal-to-noise ratio (SNR$\gtrsim 5$) yields typical statistical velocity errors of ± 50 km/s

---

[2] For our practical purposes, the difference between the photometric reference systems z and z' is negligible ($\lesssim 0.02$ mag). The derived LBT z' and FORS 2 z-band magnitudes have been confirmed to be consistent within the photometric errors. However, for easier distinction we refer to z-band magnitudes for the FORS 2 results and z' magnitudes for the deeper LBT data.

[3] http://iraf.noao.edu

Fig. 3. Cumulative radial distribution of color selected red galaxies (as in Fig. 2) as a function of cluster-centric distance (blue solid line). Dashed vertical lines indicate the radii used for color coded symbols in Fig. 2, the solid line marks the fiducial cluster radius. The dotted blue line shows the cumulative radial red galaxy number counts normalized to the enclosed area, i.e. the average red galaxy density per square arcminute within the cluster-centric distance r.

Fig. 2. *Top:* R−z color-magnitude diagram of the cluster environment based on the FORS 2 imaging data. The richly populated cluster red-sequence around the median ridgeline color R−z∼2.05 (red dashed line) is clearly visible. Filled red circles indicate objects within a 30″ radius from the X-ray center, green circles correspond to 0.5–1′, small black dots represent all other objects in the field, and open circles mark spectroscopically confirmed cluster members. Horizontal dotted lines define the applied color cut interval of ±0.2 mag about the median color, while the dotted vertical line refers to the expected apparent magnitude (m*≃21.9 mag) of a passively evolving L* galaxy at the cluster redshift (in both panels). The 50% completeness limit is indicated by the black solid line. *Bottom:* Histogram of galaxy counts in the red color interval 1.85≤R−z≤2.25 in bins of 0.4 mag for galaxies within 1′ from the cluster center (blue line). The vertical solid line indicates the nominal 50% completeness limit of the data, while the black dotted line shows the magnitude distribution for galaxies at larger distances for comparison.
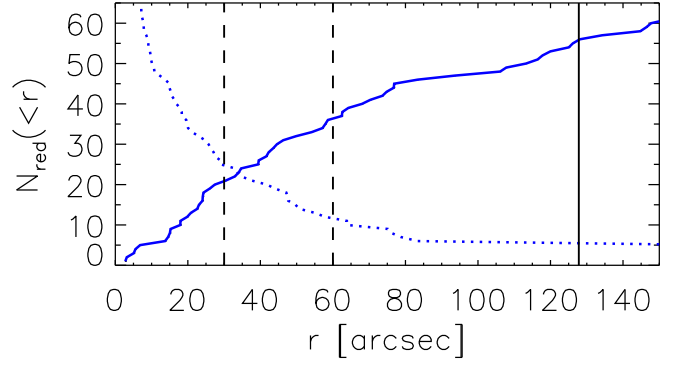
for $c \cdot z$. Adding the wavelength calibration uncertainty (≲1 Å at 8 000 Å) in quadrature, we estimate the typical uncertainty for most of the secure individual galaxy redshifts in Table 2 to be $\sigma_z \sim 0.0002$

Due to the partially poor seeing conditions, not all redshifts of targeted galaxies could be determined with high confidence. We have identified 11 additional tentative galaxy redshifts which are close to the median cluster redshift and potentially indicate member galaxies. For completeness these objects are also displayed in Fig. 5, which shows the restframe velocity distribution as a function of cluster-centric distance further discussed in Sect. 3.2.6.
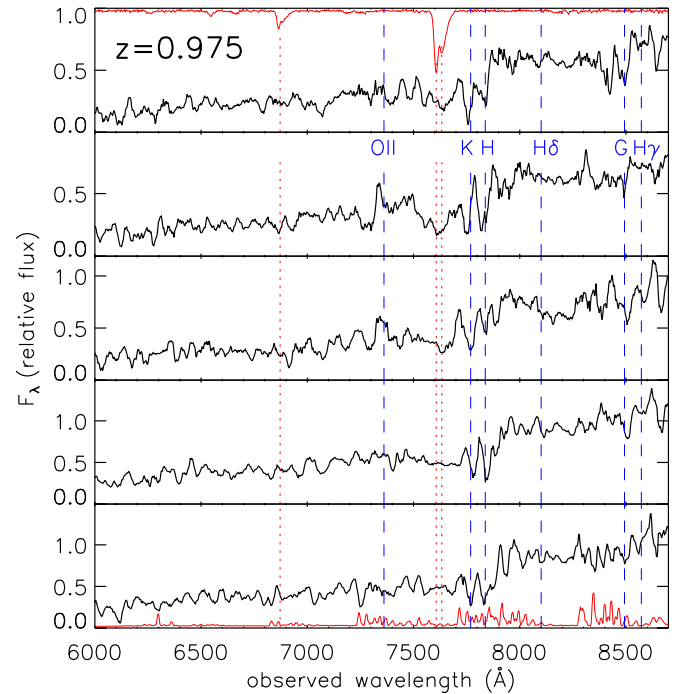
2.2. X-ray Data

2.2.1. XMM-*Newton*

XMMU J1230.3+1339 was initially detected as an extended X-ray source at high significance level in the XMM-*Newton* field with observation identification number (OBSID) 0112552101 at an off-axis angle of 4.3′ from the central target, the nearby

Fig. 4. Sample spectra of secure cluster members with the median redshift of $z = 0.975$, smoothed with a 9 pixel boxcar filter. The expected observed positions of prominent spectral features at the median redshift are indicated by blue dashed lines. The sky spectrum (bottom) and telluric features (top) are overplotted in red. From top to bottom the spectra correspond to the galaxies with object IDs 1-9-4-6-8 in Table 2.

galaxy NGC4477 in the Virgo cluster. The original XDCP source detection run, for which 470 XMM-*Newton* archival fields were processed, was performed with SAS v6.5 using the tasks `eboxdetect` and `emldetect`. With an extent likelihood of $L_{ext} \simeq 117$, corresponding to a formal probability that the source extent is due to a statistical Poissonian background fluctuation of $p_{Poisson} \simeq 1.5 \times 10^{-51}$, the cluster is one of the most significant X-ray sources among all distant cluster candidates in the XDCP survey. A detailed description of the source detection and screening procedure can be found in Fassbender (2007)
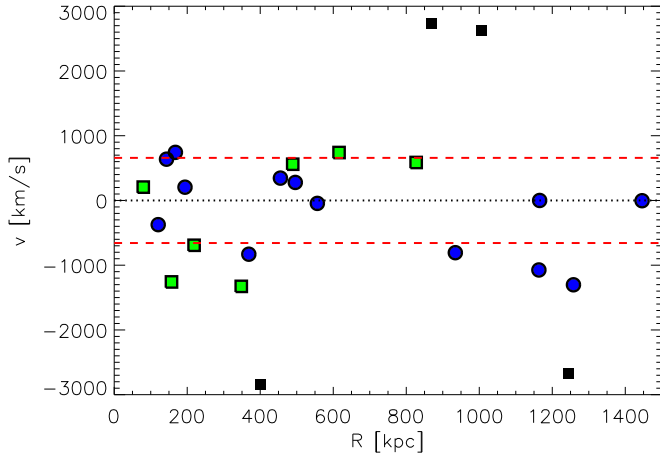
Fig. 5. Cluster restframe velocity distribution of spectroscopic cluster members as a function of projected distance from the X-ray center. Member galaxies of Table 2 with secure redshifts are indicated by blue circles, dashed lines correspond to the formal velocity dispersion estimate. For completeness, galaxies with tentative redshifts are also shown as squares, smaller black symbols indicate velocities outside the formal 3σ interval.

Table 2. Secure spectroscopic cluster members of XMMU J1230.3+1339 with total z′-band magnitudes, cluster-centric distances, and measured redshifts.

ID	RA J2000	DEC J2000	z′ mag	d_{cen} arcsec	z_{spec}
01	12:30:16.41	+13:39:16.2	20.37	15.1	0.9720
02	12:30:16.35	+13:38:49.5	19.90	18.0	0.9787
03	12:30:18.43	+13:39:06.6	21.00	21.1	0.9794
04	12:30:17.76	+13:39:26.0	20.98	24.4	0.9758
05	12:30:20.11	+13:39:00.9	21.89	46.3	0.9690
06	12:30:20.44	+13:38:38.6	20.97	57.2	0.9767
07	12:30:14.95	+13:39:58.3	21.57	62.3	0.9763
08	12:30:18.87	+13:38:00.0	20.09	69.9	0.9742
09	12:30:11.94	+13:40:33.4	20.96	117.3	0.9692
10	12:30:09.58	+13:40:38.4	23.00	146.1	0.9674
11	12:30:21.50	+13:36:54.1	21.86	146.4	0.9745
12	12:30:09.16	+13:40:49.3	21.40	158.0	0.9658
13	12:30:06.11	+13:40:22.7	22.81	181.6	0.9745

For the analysis presented here we re-processed the field with the latest version SAS v8, and additionally considered a second archival field with OBSID 0106060401 (Table 1), which encloses the cluster source at a larger off-axis angle of 9′. After applying a strict two-step flare cleaning process for the removal of high background periods, a clean net exposure time of 13.3/8.3 ksec remained for the EMOS/PN cameras in field 0112552101, and 7.8/5.0 ksec for the second observation 0106060401.

In order to optimize the signal-to-noise ratio of low surface brightness regions in the cluster outskirts discussed in Sect. 4.2, we combined the X-ray images of both XMM-*Newton* observations and their corresponding exposure maps with the SAS task `emosaic`. This results in more than 1 100 source photons from XMMU J1230.3+1339 in the mosaic image for the used 0.35-2.4 keV detection band, which provides an optimized SNR for distant cluster sources (Scharf 2002). To enable the evaluation of the significance of low surface brightness features in the presence of chip gaps, we created a signal-to-noise map of the cluster environment. Using this map, we created a log-spaced con-
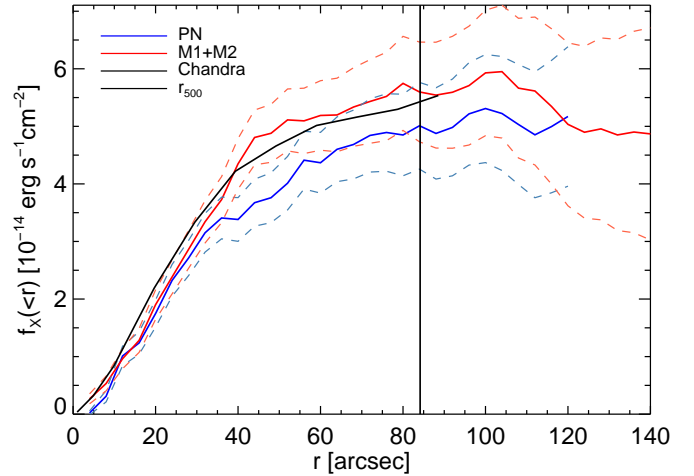
Fig. 6. Growth curve analysis for the unabsorbed, background subtracted 0.5-2 keV X-ray flux as a function of projected cluster radius. The blue solid line shows the total 0.5-2 keV flux inside the projected radius r as measured with the XMM-*Newton* PN camera, the red line represents the sum of the two MOS instruments. Poisson errors plus 5% uncertainties in the background determination are displayed by the dashed lines, the vertical line depicts the R_{500} radius. The fully consistent *Chandra* GCA result is overplotted in black. The X-ray emission can be traced out to about 90″, where it reaches the plateau value.
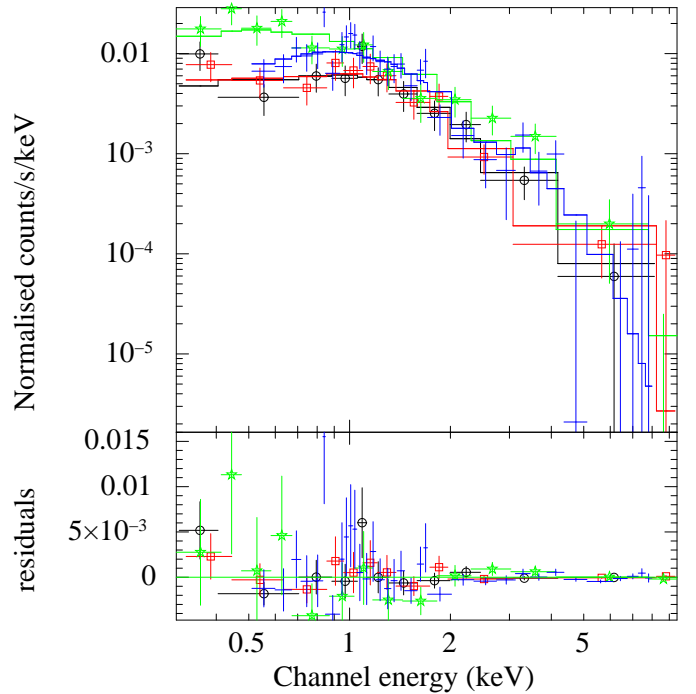
Fig. 7. *Chandra* and XMM-*Newton* X-ray spectra of XMMU J1230.3+1339 with a joint fit ICM temperature of $T_{X,2500} \simeq 5.3$ keV. The *Chandra* spectrum extracted from the ACIS-S3 chip is shown in blue, and the corresponding data from the three XMM-*Newton* instruments in green (PN), black (MOS1), and red (MOS2).

tour plot spanning the significance levels $0.5 \leq SNR \leq 35$ used in Fig. 10 of Sect. 4.2.

We applied the growth curve analysis (GCA) method of Böhringer et al. (2000) to obtain an accurate 0.5-2 keV flux measurement of the cluster as a function of radius. Since the effective exposure time and the point-spread-function (PSF) at the

cluster source are significantly better in field 0112552101, we focus the quantitative analysis on this single observation and use the second field 0106060401 only for a consistency check. Contaminating regions containing X-ray sources not associated with the cluster were conservatively masked out prior to the GCA measurement. The X-ray emission of the neighboring S0 galaxy NGC 4477 (mostly point sources) only contributes significantly at cluster-centric radii beyond 2′, i.e. the X-ray analysis of XMMU J1230.3+1339 is basically not influenced by the foreground galaxy.

Figure 6 displays the GCA results for the cluster emission, which can be traced out to a radius of about 90″, i.e. just beyond the nominal radius $R_{500} \simeq 84″$ as estimated in Sect. 3.1. Within the projected R_{500} radius we measure an unabsorbed 0.5-2 keV flux of $f_{X,500} = (5.14 \pm 0.54) \times 10^{-14}$ erg s^{-1}cm^{-2}. For completeness we also show the fully consistent *Chandra* GCA result in Fig. 6 (black line).

For the temperature determination of the cluster we followed the general procedure described e.g. in Pratt et al. (2010). As for the flux determination, we focused the spectral analysis on field 0112552101, since the effects of the broadened XMM-*Newton* PSF at larger off-axis angle outweigh the gain of additional source photons. We extracted an X-ray spectrum of the source from two circular regions of radius 40″ and 71″ centered on the X-ray peak. The smaller 40″ aperture is signal-to-noise optimized in conjunction with the *Chandra* spectral analysis, the larger aperture corresponds to the maximum radius for which reliable results can be derived with XMM-*Newton*[4]. The presence of extended thermal foreground emission from the Virgo cluster results in an increased background level[5], which we assume to be homogeneous over the cluster scale of interest of about 2′. To account for this extra foreground component, we have tested several methods with both local and external background spectrum determinations. The most robust results were obtained for the 40″ aperture using a local background spectrum extracted from a nearby uncontaminated region after the masking of point sources. With the metal abundance fixed to Z=0.3 Z$_\odot$, we derive a best fitting core region temperature for XMMU J1230.3+1339 of $5.28^{+0.90}_{-0.79}$ keV, based on a single temperature MEKAL model, a minimally binned spectrum (≥ 1 cts/bin), and C-statistics. The XMM-*Newton* spectral fit and the residuals are displayed in Fig. 7 (green, red, and black lines).

For the larger 71″ aperture, we measured a slightly higher X-ray temperature of $5.6^{+1.4}_{-1.1}$ keV applying the same local background subtraction procedure. Since this larger extraction region exhibits a lower signal-to-noise ratio and is hence more prone to background uncertainties, we cross-checked this temperature trend with an alternative spectral fitting method using an external background spectrum. In addition to the physically motivated model of the cosmic X-ray background (CXB) consisting of two unabsorbed MEKAL models plus a power law with fixed index $\gamma = 1.4$ (see Lumb et al. 2002; De Luca & Molendi 2004), we considered a further thermal MEKAL component of the total background spectrum in order to account for the local foreground emission of Virgo at the position of XMMU J1230.3+1339. From this four-component model we obtained a best fitting local Virgo temperature of $kT_{Virgo} = 1.88$ keV consistent with previous ASCA measurements of this region (Shibata et al. 2001). This four-component model, with a renormalization appropriate to the ratio of the surface area of the

---

[4] The source-flux-to-total-background-flux ratio (0.5-2 keV) is about 3:2 for the 40″ aperture and 1:2 for the 71″ aperture.

[5] The Virgo contribution to the total background is about 80%.

extraction regions, was then added to the fit of the cluster spectrum, resulting in an X-ray temperature based on this external background model of $6.4^{+1.7}_{-1.2}$ keV.

2.2.2. *Chandra*

Additional X-ray coverage of XMMU J1230.3+1339 has recently become publicly available in the *Chandra* archive, where the cluster was serendipitously observed almost on-axis in a 38.2 ksec pointing targeted on NGC 4477 (Observation ID 9527, see Tab. 1). The field was observed in `VFAINT` mode, with the cluster being located on the central ACIS-S3 detector at an off-axis angle of approximately 2′.

We performed a standard data reduction using the `CIAO v4.1` software package, with a recent version of the Calibration Database (`CALDB v4.1.1`). Since the observation was taken in `VFAINT` mode, we ran the task `acis_process_events` which provides an improved flagging of probable background events by distinguishing real X-ray photon events and events most likely associated with cosmic rays. With this procedure the ACIS particle background can be significantly reduced. The data is filtered to include only the standard event grades 0, 2, 3, 4 and 6. We confirmed that there were no flickering pixels with more than two events contiguous in time and checked visually for hot columns remaining after the standard cleaning. The resulting total net exposure time after this cleaning procedure is 37.68 ksec.

We repeated the growth curve analysis for *Chandra* in the soft 0.5-2.0 keV band (Fig. 6), which traces the cluster emission out to similar radii as in the single XMM-*Newton* field. After subtraction of the background of $b = 0.043 \pm 0.008$ cts/pixel measured in an external region 634 net cluster counts within r=2′ remain. The resulting unabsorbed *Chandra* fluxes are in full agreement with the specified XMM-*Newton* values as shown by the black line in Fig. 6.

The main advantage of the high-resolution *Chandra* X-ray data is the ability to resolve small-scale ICM structures in the inner cluster region and to obtain precise radial surface brightness (SB) profiles down to the central core. We measured the binned azimuthally-averaged surface brightness profile and performed a fit with the widely used approximation of the single isothermal β model (Cavaliere & Fusco-Femiano 1976), tracing the ICM out to about R_{500}. We fitted the functional form $S(r) = S_0(1 + (r/r_c)^2)^{-3\beta+0.5} + b$ for the radial SB profile $S(r)$ with free parameters S_0 for the central SB, r_c for the core radius, β for the slope, and a constant b for the background using a Levenberg-Marquardt least-squares minimization. The radial profile and the best fitting single β model are shown in the left panel of Fig. 8, with resulting parameters $S_0 = 0.28 \pm 0.04$ cts/pix[6], $\beta = 0.837 \pm 0.471$, $r_c = 215 \pm 110$ kpc, and a reduced-chi square of 0.70. Beyond a projected radius of about 150 kpc, the model is a very good representation of the data. The reasons for the slight deviations in the core region at $r \lesssim 50$ kpc and the flat shoulder at $r \sim 100$ kpc can be understood from a more detailed look on the cluster core region (Sect. 3.1.4) and the dynamical structure in Sect. 4.4 and Fig. 13.
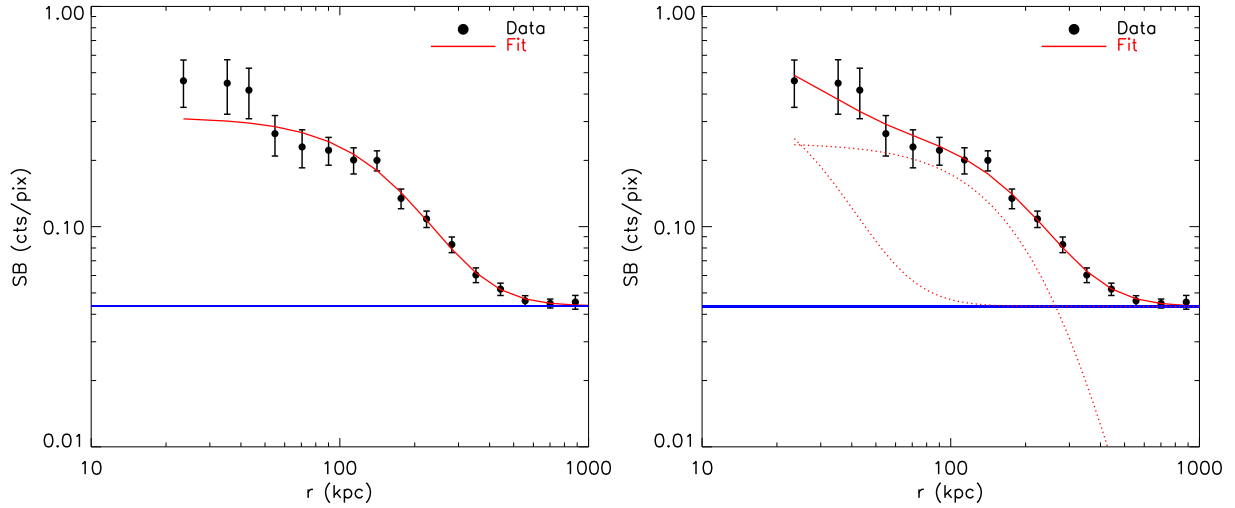
In order to obtain an improved model representation for the innermost bins of the radial profile we also performed a two-component β model fit, with a single β coefficient, but allowing for two independent core radii r_{c1} and r_{c2}

$$S(r) = S_1\left[1 + \left(\frac{r}{r_{c1}}\right)^2\right]^{-3\beta+\frac{1}{2}} + S_2\left[1 + \left(\frac{r}{r_{c2}}\right)^2\right]^{-3\beta+\frac{1}{2}} + b \,. \quad (1)$$

---

[6] Using 2x2 binned pixels with an effective scale of 0.984″ per pixel.

Fig. 8. *Chandra* surface brightness profile of XMMU J1230.3+1339 (black data points) with the best fitting single (*left*) and two-component (*right*) beta models (red solid lines). The background level is indicated by the blue line. The dotted lines in the right panel represent the individual fit components, the inner one includes the background and the outer one is additive.

The resulting fit parameters for this model are $\beta = 1.0$ (the maximum allowed value), $S_1 = 0.42 \pm 0.51$ cts/pix, $r_{c1} = 42 \pm 34$ kpc, $S_2 = 0.24 \pm 0.04$ cts/pix, and $r_{c2} = 272 \pm 32$ kpc with a reduced-chi square equal to 0.45 As shown in the right panel of Fig. 8, the core region of the SB distribution at $r \lesssim 100$ kpc is now qualitatively better modelled.

We also measured the surface brightness concentration for the cluster using the parameter $c_{SB} = (SB[r < 40\,\mathrm{kpc}])/(SB[r < 400\,\mathrm{kpc}])$ as defined by Santos et al. (2008), which allows an improved structural characterization of high-z clusters compared to methods requiring very high photon statistics. For XMMU J1230.3+1339 this parameter is found to be $c_{SB} = 0.07$, which places the system in the formal category of Non-Cool Core (NCC) clusters, in contrast to the more centrally concentrated objects in the moderate and strong Cool Core Cluster (CCC) class at high redshift (Santos et al. 2008).

For the visual representation of the two dimensional X-ray surface brightness structure (Figs. 1, 9, and 13), we adaptively smoothed the *Chandra* soft band image and created an X-ray contour map with eight log spaced surface brightness levels spanning the significance range of 1-70 σ above the background rms. It should be noted that the cluster does not contain any detectable point sources within R_{500} at the current *Chandra* depth. The structural and spectral analysis of the cluster properties should thus be unbiased, also for XMM-*Newton* with its lower spatial resolution.

We performed a spectral temperature fit in a signal-to-noise optimized aperture of 40″ following the procedure described in Tozzi et al. (2003). Applying the same general procedure as for XMM-*Newton* with the local background measured in an on-chip region with 60″ diameter, we obtain a best fitting *Chandra* core temperature of $5.40^{+1.27}_{-0.94}$ keV with the abundance fixed at $0.3\,Z_\odot$. The spectrum and model fit is displayed in blue in Fig. 7, which also shows an indication of the Fe line at $kT \sim 3.3$ keV. Leaving the metal abundance as a free parameter, we can derive a weak *Chandra*-only core region constraint of $Z = 0.46^{+0.38}_{0.28}\,Z_\odot$.

3. Results and mass estimates

In the following section we will present results derived from the X-ray measurements and the optical imaging and spectroscopic data. A special focus will be given to a range of observables that are commonly used as proxies for the cluster mass. All final M_{200} cluster mass estimates (ME) based on a given observable are labelled with a number (e.g. ME 1) for the purpose of easier referencing, intermediate results are indicated by an additional letter (e.g. ME 1a, ME 1b). All used mass-observable scaling relations are stated explicitly for clearness, transformed into our assumed cosmology and the used cluster mass definition M_{200}, where applicable.

3.1. Global X-ray properties

We will start with the X-ray determined bulk properties of the intracluster medium in order to establish some first robust fundamental characteristics of the cluster. For all subsequent discussions, we define the 'center-of-mass' of the ICM X-ray emission determined with XMM-*Newton* (RA=12:30:16.9, DEC=+13:39:04.3, see Tab. 3) as the reference center of the cluster, and measure all cluster-centric distances relative to this point.

3.1.1. X-ray temperature

The *Chandra* and XMM-*Newton* results on the ICM temperature in the 40″ aperture core region are of comparable statistical quality and are fully consistent with each other. In order to further decrease the uncertainties, we have performed a joint *Chandra*/XMM-*Newton* spectral fit to these data for the region within $40'' \cong R_{2500}$ (see below). We find a final joint X-ray temperature of $kT_{X,40''} \simeq kT_{X,2500} = 5.30^{+0.71}_{-0.62}$ keV (see Fig. 7) using the same method as in Sect. 2.2 with a fixed metallicity of $Z = 0.3\,Z_\odot$, minimally binned data, and C-statistics. Leaving the metallicity as a free parameter, we can constrain the iron abundance in the cluster core to $Z_{2500} = 0.43^{+0.24}_{-0.19}\,Z_\odot$, i.e. with a 2.3 σ detection significance.

The XMM-*Newton* data analysis indicates that the global ICM temperature of XMMU J1230.3+1339 is higher when the measurement aperture is increased. With the currently available X-ray data set this is a tentative trend, as the measurement errors also increase. However, to allow for an evaluation of possible biases, we take the average of the 71″ temperatures (local and external background) as a second reference temperature $kT_{X,71''} \simeq 6.0^{+1.6}_{-1.2}$ keV. Since ideally one would like to have a measurement of $T_{X,500}$, i.e. within the full R_{500} region, the latter value in the 6 keV range could indeed be a better approximation of the underlying global temperature of the cluster.

This global X-ray temperature is the fundamental parameter of the intracluster medium and is closely linked to the depth of the underlying potential well of the cluster through the Virial theorem. We use the jointly determined best (core) X-ray temperature $T_{X,2500}$ with an uncertainty of about ±13% to derive robust size measures of the cluster, which is an important prerequisite for the measurement of most cluster related quantities. We are using the R-T scaling relations of Arnaud et al. (2005), which have been calibrated using a local cluster sample based on high-quality XMM-*Newton* data[7]. Using the R-T scaling relation for hot systems ($T_X > 3.5$ keV) $R_{200} = (1714 \pm 30) \times E^{-1}(z) \times (kT/5\,\text{keV})^{0.50\pm0.05}$ kpc, we obtain for XMMU J1230.3+1339 an estimated $R_{200} = 1017^{+68}_{-60}$ kpc. For R_{500}, using the normalization 1129 ± 17 kpc of the R-T relation, the estimated radius is $R_{500} = 670^{+45}_{-39}$ kpc, and similarly $R_{2500} = 297^{+20}_{-17}$ kpc (normalization 500 ± 5 kpc). Standard error propagation was applied in all cases to evaluate the uncertainties. In terms of projected distance in the plane of the sky at the cluster redshift, these representative length scales correspond to angular distances of [R_{200}, R_{500}, R_{2500}]=[127.8″, 84.2″, 37.3″]. With respect to the higher temperature estimate $T_{X,71''}$, all derived radii would increase by about 6%, i.e. possible systematic effects are mostly small in comparison to other uncertainties.

As the next step, we can derive a first mass estimate of the cluster by using the M-T relation of Arnaud et al. (2005), calibrated with the same local cluster sample as above. Using again the best joint temperature $T_{X,2500}$, we obtain from the relation

$$M^{T_X}_{200} = \frac{(5.74 \pm 0.30)}{E(z)} \times \left(\frac{kT}{5\,\text{keV}}\right)^{1.49\pm0.17} \times 10^{14}\,\text{M}_\odot \quad (2)$$

an estimate of the approximate total mass of the cluster of $M_{200} = 3.61^{+0.77}_{-0.68} \times 10^{14}\,\text{M}_\odot$ (ME 1a). For M_{500} the M-T relation, with the normalization of $(4.10 \pm 0.19) \times 10^{14}\,\text{M}_\odot$, yields $M_{500} = 2.58^{+0.54}_{-0.48} \times 10^{14}\,\text{M}_\odot$.

The use of the higher temperature estimate $T_{X,71''}$ translates into a 20% higher mass of $M_{200} \simeq 4.34 \times 10^{14}\,\text{M}_\odot$ (ME 1b). We take this positive offset of $0.73 \times 10^{14}\,\text{M}_\odot$ into account as a potential systematic error (denoted in brackets) and arrive at a final X-ray temperature-based mass estimate of $M^{T_X}_{200} = 3.61^{+0.77(+0.73)}_{-0.68} \times 10^{14}\,\text{M}_\odot$ (ME 1).

One of the main objectives of this work is the comparison of total cluster mass estimates, most commonly approximated by M_{200}, as derived from various mass-observable relations. For scaling relations calibrated to yield only M_{500}, we apply the ratio of the normalizations of the respective M-T relations (see above) $f_{500\rightarrow200} = M_{200}/M_{500} \simeq 1.40$ to obtain a total mass estimate M_{200}. In the same way, $f_{2500\rightarrow200}$ is given by $f_{2500\rightarrow200} = M_{200}/M_{2500} \simeq 3.21$.

---

[7] Temperatures in Arnaud et al. (2005) are determined in the region $[0.1–0.5]R_{200}$. The effect of using $T_{X,2500}$ for this work should be small and is accounted for by the discussed systematics.

3.1.2. Hydrostatic mass estimate

Under the assumption of an ideal isothermal gas in hydrostatic pressure equilibrium (HE), the following widely used approximation for the total mass profile can be derived (e.g. Hicks et al. 2008; Rosati et al. 2009)

$$M^{\text{HE}}_{\text{tot}}(<r) \simeq \frac{3\,k_B}{G\,\mu\,m_p} \cdot T \cdot \beta \cdot \frac{r \cdot \left(\frac{r}{r_c}\right)^2}{1 + \left(\frac{r}{r_c}\right)^2} \quad (3)$$

$$\simeq 1.13 \cdot \beta \cdot \left(\frac{T}{1\,\text{keV}}\right)\left(\frac{r}{1\,\text{Mpc}}\right)\frac{\left(\frac{r}{r_c}\right)^2}{1 + \left(\frac{r}{r_c}\right)^2} \times 10^{14}\,\text{M}_\odot ,$$

where k_B is the Boltzmann constant, G the gravitational constant, m_p the proton mass, and $\mu \simeq 0.59$ the mean molecular weight in atomic mass units. By using the joint X-ray temperature $T_{X,2500}$, and the single beta model fit parameters from *Chandra* ($\beta \simeq 0.84$, $r_c \simeq 215$ kpc), we obtain the hydrostatic mass estimates for XMMU J1230.3+1339 of $M_{500} \simeq 3.1\times10^{14}\,\text{M}_\odot$ and $M_{200} \simeq 4.9\times10^{14}\,\text{M}_\odot$ (ME 2a), whereas the latter value is slightly extrapolated beyond the last reliable data point of the measured X-ray SB profile.

Note that only about 11% (18%) of the total mass M_{200} (M_{500}) is actually enclosed within one core radius r_c, within which the single beta model exhibits some deviations from the data possibly due to the onset of cooling (see Sect. 3.1.4) and significant dynamical activity (see Sect. 4.4). Between one core radius and $r \gtrsim R_{500}$ the model describes the radial surface brightness profile with good accuracy, so that an extrapolation out to R_{200} is justified. The dominant source of uncertainty here is the ~56% error on the β parameter due to a degeneracy with the fitted core radius over the accessible data range. Taking this and the temperature and radii errors into account we arrive at a final hydrostatic equilibrium mass estimate of $M^{\text{HE}}_{200} = (4.9 \pm 2.8) \times 10^{14}\,\text{M}_\odot$ (ME 2).

3.1.3. X-ray luminosity

From an observational point of view, the X-ray luminosity L_X is the ICM bulk property which is easiest to determine, as it only requires flux and redshift measurements. For this reason, the X-ray luminosity is of crucial importance for most large-scale X-ray surveys and provides the link to other ICM properties and the total cluster mass (e.g. Reiprich & Böhringer 2002) via L_X scaling relations.

For XMMU J1230.3+1339 we determine a restframe 0.5-2 keV cluster luminosity of $L^{0.5-2\,\text{keV}}_{X,500} = (1.92 \pm 0.20)\times10^{44}$ erg/s within the accessible aperture R_{500}. The bolometric X-ray luminosity can be determined by applying a temperature dependent bolometric correction factor $f^{\text{bol}}_{0.5-2\,\text{keV}}$ to the soft band luminosity (e.g. Böhringer et al. 2004), in our case $f^{\text{bol}}_{0.5-2\,\text{keV}} \simeq 3.38$, yielding a total bolometric [0.01-100 keV] luminosity for the cluster of $L^{\text{bol}}_{X,500} = f^{\text{bol}}_{0.5-2\,\text{keV}} \cdot L^{0.5-2\,\text{keV}}_{X,500} = (6.50 \pm 0.68)\times10^{44}$ erg/s.

Recently the use of a core-excised X-ray luminosity has been shown to reduce the scatter in the L_X scaling relations by a factor of 2 (Pratt et al. 2009), simply by avoiding the central cluster region and its related complex physical processes. For XMMU J1230.3+1339 we measure a core-excised luminosity in an aperture of $[0.15-1]R_{500}$ of $L^{0.5-2\,\text{keV}}_{X,[0.15-1]500} = (1.53 \pm 0.21)\times 10^{44}$ erg/s.

Pratt et al. (2009) also provide the latest L_X scaling relations calibrated with the representative local REXCESS sample (Böhringer et al. 2007). Applying the self-similar L-T relation[8] $E^{-1}(z) \cdot L_{X,500}^{\text{bol}} = (7.13 \pm 1.03)(kT/5\,\text{keV})^{3.35 \pm 0.32} \times 10^{44}$ erg/s, we would predict an X-ray temperature for the cluster of $\simeq 4.1$ keV, i.e. a value approximately 2σ below our spectroscopic temperature measurement. The main reason for this discrepancy is the assumption of self-similar evolution of the X-ray luminosity, i.e. $L_X \propto E(z)$ at fixed temperature. While some empirical results at $z \lesssim 1$ are consistent with this evolutionary scenario (e.g. Vikhlinin et al. 2002; Kotov & Vikhlinin 2005; Maughan et al. 2006), other studies extending towards higher redshifts find little or no evolution (e.g. O'Hara et al. 2007; Rosati et al. 2002), or even negative trends with redshift (Ettori et al. 2004). XMMU J1230.3+1339 by itself would be consistent with either of the latter two scenarios. Since the evolutionary trends of the X-ray luminosity at high redshifts ($z > 0.8$) are not well constrained yet, we assume as a starting point a no-evolution scenario, which would predict $T_X \simeq 4.9$ keV for the given luminosity, and treat a possible L_X redshift evolution as a systematic uncertainty. The use of a no-evolution scenario for the L-T relation instead of the self-similar prediction is also empirically supported by the latest compilation of high-z cluster measurements (Reichert et al., in prep.).

With this assumption on the evolution of L_X, we can derive an additional mass estimate of the cluster based on the L-M relation of Pratt et al. (2009)

$$\frac{L_{X,500}^{\text{bol}}}{E^{\frac{4}{3}}(z)} = (1.38 \pm 0.12)\left(\frac{M_{500}}{2 \times 10^{14}\,\text{M}_\odot}\right)^{2.08 \pm 0.13} \times 10^{44}\,\text{erg/s}, \quad (4)$$

corrected for one factor of $E(z)$ to take out the self-similar redshift scaling[9] (in L-T). We thus obtain a mass estimate of $M_{500} \simeq (2.96 \pm 0.41) \times 10^{14}\,\text{M}_\odot$ from the L-M relation, which yields $M_{200} \simeq f_{500 \to 200} \cdot M_{500} \simeq (4.1 \pm 0.6) \times 10^{14}\,\text{M}_\odot$ (ME 3a). However, the dominant uncertainty in this luminosity-based mass proxy is the discussed weak constraint on the luminosity evolution. We take this current lack of knowledge into account by adding a 23% systematic error, based on the decreased mass estimate of the self-similar evolution model. The final luminosity-based total mass estimate is hence $M_{200}^{L_X} \simeq (4.1 \pm 0.6\,(\pm 1.0)) \times 10^{14}\,\text{M}_\odot$ (ME 3). Using the core excised X-ray luminosity $L_{X,[0.15-1]500}^{0.5-2\,\text{keV}}$ with the corresponding scaling relation yields a consistent mass estimate within 8%, implying that the central region of XMMU J1230.3+1339 does not exhibit any particular feature that would drive a deviation.

3.1.4. Core properties of the ICM

We now have a more quantitative look at the properties of the intracluster medium in the densest central core region. The line-of-sight emission measure $\text{EM} = \int n_e^2\, dl = 4\pi\,(1+z)^4\,S(r)/\Lambda(T,z)$ gives direct observational access to the local electron density n_e, deduced from the deprojected measured surface brightness profile $S(r)$ as a function of cluster-centric distance r in the soft X-ray band, and the redshifted and absorption corrected cooling function $\Lambda(T,z)$. For an assessment of the central density of the cluster, we use the double beta model surface brightness fit (right panel of Fig. 8), since the inner beta model component

dominates the densities within the central 40 kpc. After the de-projection of the SB model fits (S_1, r_{c1}, S_2, r_{c2}, β) of Sect. 2.2.2, we obtain a total electron density of $n_{e,0} \simeq (2.3 \pm 1.4) \times 10^{-2}\,\text{cm}^{-3}$ in the very center, and $n_{e,20\,\text{kpc}} \simeq (1.7 \pm 1.0) \times 10^{-2}\,\text{cm}^{-3}$ at a cluster-centric radius of 20 kpc.

The central density and temperature of the ICM determine the cooling time scale t_{cool} in the cluster core (Sarazin 1986), i.e. the time for which the thermal energy of the gas would be radiated away at the current cooling rate

$$t_{\text{cool}} \simeq 2.9 \times 10^{10}\,\text{yr} \cdot \left(\frac{n}{10^{-3}\,\text{cm}^{-3}}\right)^{-1}\left(\frac{kT}{1\,\text{keV}}\right)^{1/2}. \quad (5)$$

From this expression we derive a central cooling time scale[10] for XMMU J1230.3+1339 of $t_{\text{cool,0}} = (2.9 \pm 1.8)$ Gyr and at the 20 kpc radius $t_{\text{cool,20kpc}} = (4.0 \pm 2.4)$ Gyr. This time scale is to be compared to the age of the Universe at the redshift of the cluster ($t \simeq 5.85$ Gyr), or for more realistic cluster formation scenarios, the time span since $z = 3$ ($t \simeq 3.74$ Gyr) or $z = 2$ ($t \simeq 2.63$ Gyr).

The central electron density $n_{e,0}$ provides an alternative test for the presence of a cool core. Following the CCC definition of Pratt et al. (2009) ($n_{e,0} > 4 \times 10^{-2} \cdot E^2(z)\,\text{cm}^{-3}$), XMMU J1230.3+1339 is consistently classified as a Non-Cool-Core cluster, in concordance with the surface brightness concentration measure c_{SB} in Sect. 2.2.2. However, the cluster's core region is in an interesting transition phase, where the dense gas has basically been going through a single full cooling time scale since redshift 2-3. Hence, the central core region could indeed contain gas which has already cooled considerably, consistent with our tentative finding of an increasing average X-ray temperature with radius in Sect. 3.1.1.

3.1.5. Gas mass

The total gas mass M_{gas} of clusters is obtained from the integrated radial gas density profile. For XMMU J1230.3+1339, both the deprojected single beta model ($n_{e,0} \simeq 0.71 \times 10^{-2}\,\text{cm}^{-3}$, $\beta \simeq 0.84$, $r_c \simeq 215$ kpc) and the double beta model yield consistent results for the gas mass of $M_{\text{gas,500}} \simeq (3.0 \pm 0.9) \times 10^{13}\,\text{M}_\odot$, where the estimated error is based on the uncertainties of the latter model in combination with the allowed temperature range.

Using the mean local gas mass fraction for similarly massive clusters of $\bar{f}_{\text{gas,500}} \simeq 0.10 \pm 0.02$ (Pratt et al. 2009), we readily obtain a fourth total mass estimate of $M_{200}^{\text{gas}} \simeq f_{500 \to 200} \cdot M_{\text{gas,500}}/\bar{f}_{\text{gas,500}} \simeq (4.2 \pm 1.5) \times 10^{14}\,\text{M}_\odot$ (ME 4).

With the knowledge of the final combined best estimate for the total cluster mass M_{200}^{best} as discussed in Sect. 5.2, we can turn the argument around and estimate the cluster gas mass fraction for XMMU J1230.3+1339 for the assumed cosmology. This consistency check yields $f_{\text{gas,500}} \simeq M_{\text{gas,500}}/(M_{200}^{\text{best}}/f_{500 \to 200}) \simeq 0.100 \pm 0.035$ in good agreement with the average local value.

3.1.6. Y_X

As the final *Chandra* and XMM-*Newton* derived property, we determine the X-ray version of the Compton-Y parameter $Y_X = M_{\text{gas}} \cdot T_X$. This quantity reflects the total thermal energy of the ICM and is predicted to be a robust, low scatter mass proxy from simulations (e.g. Kravtsov et al. 2006; Nagai et al. 2007) which has recently been well confirmed by observations (e.g. Arnaud et al. 2007; Vikhlinin et al. 2009a; Arnaud et al. 2010).

---

[8] Derived with the BCES orthogonal fit method and corrected for Malmquist bias.

[9] This approach is somewhat ad hoc at this point, but provides a significantly improved agreement with other high-z cluster measurements.

[10] When considering only the single β-model fit parameters, this cooling time scale increases by a factor of 3.

From the measurements of the global X-ray temperature and the gas mass within the radius R_{500}, we obtain $Y_{X,500} = (1.6 \pm 0.5\,(+0.2)) \times 10^{14}\,M_\odot$ keV, where again a systematic error is considered for a possible temperature bias (Sect. 3.1.1). With the latest calibration of the M-Y_X scaling relation from Arnaud et al. (2010) we find

$$M_{500} = \frac{10^{14.567 \pm 0.010}}{E^{\frac{2}{3}}(z)} \left(\frac{Y_X}{2 \times 10^{14}\,M_\odot\,\text{keV}} \right)^{0.561 \pm 0.018} M_\odot \qquad (6)$$

$$\simeq (2.6 \pm 0.8\,(+0.3)) \times 10^{14}\,M_\odot \,,$$

and hence $M_{200}^{Y_X} \simeq f_{500 \rightarrow 200} \cdot M_{500} \simeq (3.6 \pm 1.1\,(+0.4)) \times 10^{14}\,M_\odot$ (ME 5).

3.2. Optical properties

We now turn to the optical cluster properties as derived from the VLT/FORS2 imaging and spectroscopic data and the wide-field multi-band LBT imaging observations.

The rich galaxy population of XMMU J1230.3+1339 is easy to recognize when inspecting the top panels of Fig. 1, either as a galaxy overdensity measure in the single band (left panel), or in color space (right), where the red early-type cluster galaxies clearly stand out from the foreground/background. An interesting note is the fact that the angular size of the foreground Virgo galaxy NGC 4477 is almost identical to the cluster total radius. At a projected cluster-centric distance of about 700 kpc towards the West, the optical light of the NGC 4477 halo starts to significantly contaminate the colors of background galaxies, and at >850 kpc in this Western direction the region is basically masked out by the foreground elliptical. The proximity of the cluster to NGC 4477 hence has two effects on the optical analysis: (i) galaxy counts have to be corrected for the geometrically covered area in the outer regions, and (ii) the measured colors of galaxies overlapping with the outer halo of NGC 4477 are likely biased towards the blue.

Throughout this Sect. 3.2 we are facing the task to appropriately re-scale measurement apertures that were defined in the local Universe to be applicable at $z \sim 1$. This is not a straightforward exercise, since (i) one has to distinguish fixed-size physical apertures from relative cluster apertures that evolve with redshift, and (ii) this evolution depends on the reference density relative to which all cluster quantities are defined. For the overdensity definition with respect to the critical density $\rho_{cr}(z)$, used in this work, the radius scales in the self-similar model for a cluster at fixed mass as $r \propto E^{-2/3}(z)$ (e.g. Voit 2005), i.e. it changes by a factor of 1.44 from $z = 0$ to the cluster redshift. On the other hand, a definition relative to the mean density $\rho_{mean}(z)$ implies a scaling of $r \propto (1 + z)^{-1}$, i.e. a decrease by 1.98, and with reference to the top-hat collapse density $\Delta(z)$ radii scale as $r \propto E^{-2/3}(z) \cdot \Delta^{-1/3}(z)$, equivalent to a shrinking by about a factor of 1.67 at the cluster redshift. For the following discussion we choose an intermediate radius re-scaling approach consistent with Carlberg et al. (1997) $r \propto E^{-1}(z)$, i.e. where appropriate we apply a radius correction factor of $f_{resc} = 1/E(z) \simeq 0.58$. Since the total enclosed mass close to the outer radius scales approximately as $M_{tot}(< r) \propto r$ (see e.g. Equ. 3), the use of different re-scaling approaches for the measurement aperture of optical quantities can lead to systematic total mass shifts of ± 15-20%. Working with fixed physical apertures, on the other hand, could result in an overestimation of the total cluster mass by up to a factor of 2 at $z \sim 1$, when using optical observables such as richness or total luminosity.

3.2.1. Richness measures

As starting point, we determine the classical optical richness measure, the Abell richness R^{rich} (Abell 1958), defined as the number of cluster galaxies within the projected Abell radius $R_A \simeq 2.14\,h_{70}^{-1}$ Mpc and with apparent magnitudes in the interval $[m_3, m_3 + 2]$, where m_3 is the third brightest cluster galaxy. We use the LBT/LBC z'-band as the reddest optical wide-field imaging filter, providing the highest cluster-to-foreground/background contrast and allowing background estimations in the same field. The magnitude interval for the Abell richness in our case is $[m_{3,z}, m_{3,z} + 2] = [20.74, 22.74]$, and for the re-scaled Abell radius we assume $R_{A,resc} \simeq f_{resc} \cdot R_A \simeq 1240$ kpc, corresponding to an angular scale of 156''.

We determined the statistical background/foreground galaxy counts in this magnitude interval in 17 external background regions with a radius equivalent to R_{500} each, yielding a median z'-band field galaxy density of 8.4 ± 1.5 arcmin^{-2}. For the cluster region within R_{500}, which is not influenced by NGC 4477, we obtain a galaxy overdensity of (74 ± 9). The richness estimate for the scaled Abell radius $R_{A,resc}$ is then (109 ± 17), after applying a 10% correction (~3 galaxies) for the geometrically covered area in the outer ring beyond R_{500}. This implies that XMMU J1230.3+1339 falls in the Abell richness class $R^{rich} = 2$, defined as having 80-129 counted galaxy members, and would thus rank among the top 20% of the richest clusters even in the local Abell catalog.

A more modern and better calibrated richness measure is N_{200} (Koester et al. 2007b; Reyes et al. 2008), the number of E/S0 ridgeline member galaxies within R_{200}, fainter than the BCG and brighter than $0.4\,L*$. This richness definition has been used for the MaxBCG catalog of Koester et al. (2007a) of optically selected groups and clusters from the Sloan Digital Sky Survey (SDSS) in the redshift range $0.1 < z < 0.3$. We follow Reyes et al. (2008) for a self-consistent procedure to determine N_{200}, which has been used and calibrated with a different definition of R'_{200}, evaluated relative to the mean density ρ_{mean} of the Universe. For the selection of E/S0 ridgeline galaxies we use the color cuts R$-$z$=2.05 \pm 0.2$ as shown in Fig. 2, with a comparable color width as used for the MaxBCG catalog. The considered z-band magnitude range is then [19.9 mag, 22.9 mag], confined by the measured BCG magnitude and a SSP (Simple Stellar Population) model magnitude of a $0.4\,L*$ galaxy at the cluster redshift (see below). For the iterative process, we first determine the number of galaxies fulfilling the color and magnitude cuts within a fixed projected radius of $1\,h^{-1}$ Mpc $\simeq 1.43$ Mpc yielding $N_{1\,h^{-1}\,\text{Mpc}} = 56$. From the very similar scaled final search radius $R_{200}^* \simeq 0.223\,N_{1\,\text{Mpc}}^{0.6} \cdot f_{resc}\,h_{70}^{-1}$ Mpc $\simeq 1.44$ Mpc[11], we obtain the final richness measure $N_{200} \simeq 57$, which again includes a small correction (3 galaxies) for the region covered by NGC 4477.

A total mass estimate based on this richness estimate is then obtained from the calibrated MaxBCG scaling relation of Reyes et al. (2008). Due to different radius definitions, the cluster mass M'_{200} resulting from this scaling relation is systematically higher than M_{200} used in this work. In the local Universe M'_{200} is about 40% larger, which reduces to approximately 8% at $z \sim 1$, due to the fact that $\rho_{mean}(z)$ converges to $\rho_{cr}(z)$ with increasing redshift. For consistency with our M_{200} mass definition we apply a correction factor $f_{cr}^{mean}(z \sim 1) \simeq 0.92$ and convert the mass units to $h_{70}^{-1} M_\odot$

---

[11] Note that the optically defined radius R_{200}^* for the determination of N_{200} and L_{200} is different from the T_X derived radius R_{200} used throughout most of the paper.

$$M_{200}^{N_{200}} = f_{\mathrm{cr}}^{\mathrm{mean}} \cdot (2.03 \pm 0.11) \cdot \left(\frac{N_{200}}{20}\right)^{1.16 \pm 0.09} \times 10^{14} \mathrm{M}_\odot \qquad (7)$$

$$\simeq (6.3 \pm 0.7) \times 10^{14}\,\mathrm{M}_\odot\,.$$

In terms of systematic uncertainties, we consider an additional $\pm 15\%$ error for the aperture re-scaling, and $\pm 20\%$ for the selected color cuts and possible foreground/background contamination in the richness estimate. Furthermore, all optical scaling relations in Reyes et al. (2008) are derived from stacked cluster quantities, i.e. they do not contain the information on the scatter of individual clusters with respect to the best fitting relation. To account for this intrinsic scatter, we add a conservative minimum of $\pm 20\%$ systematic mass uncertainty to all optical mass proxies (see e.g. Popesso et al. 2005). With a combined possible systematic mass offset of $\pm 32\%$, the final richness based total mass estimate is hence $M_{200}^{N_{200}} \simeq (6.3 \pm 0.7\,(\pm 2.0)) \times 10^{14}\,\mathrm{M}_\odot$ (ME 6).

3.2.2. Brightest Cluster Galaxy

We address the characteristics of the Brightest Cluster Galaxy (BCG) of XMMU J1230.3+1339 and compare them to predictions from Simple Stellar Population (SSP) models. The BCG can be readily identified in the color-magnitude-diagram in Fig. 2 as the galaxy with total z-band magnitude $z_{\mathrm{tot}}^{\mathrm{BCG}} = 19.90$ and a color of R−z≃2.04. In the lower left panel of Fig. 1 the BCG is marked by a green dashed circle at a projected offset from the nominal X-ray center of about $18''$ corresponding to 140 kpc. Furthermore, the BCG (ID02 in Table 2) seems not to be at rest in the cluster reference system, but rather exhibits a velocity of about +600 km/s with respect to the median redshift. The lower panels of Fig. 1 also reveal that the BCG has a very close companion galaxy with a consistent color in the projected view, which could be an indication for on-going or upcoming merging activity. We can summarize, that XMMU J1230.3+1339 has a dominant BCG in the cluster core with properties in the CMD (magnitude, color, luminosity gap) very similar to most local clusters, but additional characteristics (cluster center offset, cluster velocity offset, close companion) that point towards a dynamical BCG state which is yet to reach a final equilibrium configuration at the minimum of the cluster potential well.

Interestingly, we can identify a second galaxy with BCG properties on the outskirts of the cluster, from now on referred to as BCG2 for distinction. This galaxy can be seen in the Southern half of Fig. 1 (top right panel) and in Fig. 11. The BCG2 spectrum is shown in the lower panel of Fig. 4 and further properties are specified in Table 2 (ID08). With a total magnitude of $z_{\mathrm{tot}}^{\mathrm{BCG2}} = 20.1$, the BCG2 is only 0.2 mag fainter than the core BCG and has a slightly bluer color in comparison. Due to the projected distance of about $70'' \simeq 550$ kpc from the cluster center, the BCG2 appears in the CMD of Fig. 2 as a spectroscopically confirmed (open circle) non-core member (small black dot). The cluster restframe velocity of the BCG2 is consistent with zero, giving rise to the conclusion that the BCG2 has just entered the R_{500} region of the cluster approximately along the plane of the sky, which will be further discussed in Sect. 4.2.2.

The comparison to stellar population synthesis models allows us to probe in more detail the BCG properties and to compare them with observations in the local Universe. We have computed a grid of SSP models using PEGASE2 (Fioc & Rocca-Volmerange 1997) with different formation redshifts and metallicities for relating them to the observed redshift evolution of

passively evolving galaxies (for details, see Fassbender 2007). The observed R−z color is well matched by a model with a single star formation burst at $z_f \simeq 5$ and slightly supersolar metallicity for the BCG and about solar metallicity for BCG2. For $z \sim 1$, our models further predict an apparent magnitude of $z \simeq 21.9$ mag for a passive L* galaxy, implying that the BCG has a luminosity of $\simeq 6.5$ L* (or m*-2).

For the comparison of passive galaxy luminosities at higher-z to local measurements such as MaxBCG, two different approaches could in principle be followed. The first option is to perform the measurements in the same observed band, r in the case of MaxBCG, and then account for passive evolution and a K-correction term of order 2 mag using the model predictions. The observationally preferable second approach uses the best suited band for the measurement, z in our case, then applies significantly smaller evolution and K-correction terms, and finally transforms the local values into the desired reference band using the model. Here we follow the latter method in order to take advantage of the ~2 magnitudes brighter passive cluster galaxies in the z-band compared to r or R.

We determine the absolute z-magnitude by applying the distance modulus equation $m_{\mathrm{BCG}}(z) - M_{\mathrm{BCG}} = 25 + 5\log(d_{\mathrm{lum}}\,[\mathrm{Mpc}]) + K_{\mathrm{BCG}}(z)$. With $z_{\mathrm{tot}}^{\mathrm{BCG}} = 19.90$, the luminosity distance $d_{\mathrm{lum}} = 6403.6$ Mpc, and a K-correction of $K_{\mathrm{BCG}} \simeq 0.82$ we obtain $M_{\mathrm{BCG}}^z = -24.95 \pm 0.03$ mag for our assumed concordance cosmology. Using the absolute magnitude of the sun $M_\odot^z = 4.51$ (Blanton et al. 2003) we can derive the BCG luminosity as $L_{\mathrm{BCG}}^z \simeq 6.1 \times 10^{11}$ L$_\odot$.

The BCG luminosity is known to correlate weakly with the cluster mass (Lin & Mohr 2004). Although found to be a fairly poor tracer of M_{200}, Reyes et al. (2008) provide a calibrated L_{BCG}-M scaling relation for BCG r-band luminosities evaluated and K-corrected at $z = 0.25$. With the discussed correction term $f_{\mathrm{cr}}^{\mathrm{mean}}$ and luminosities and masses transformed to h_{70}^{-2} L$_\odot$ and h_{70}^{-1} M$_\odot$ we arrive at the following relation

$$M_{200}^{L_{\mathrm{BCG}}} = f_{\mathrm{cr}}^{\mathrm{mean}}(1.53 \pm 0.10)\left(\frac{L_{\mathrm{BCG}}^r}{1.02 \times 10^{11} \mathrm{L}_\odot}\right)^{1.10 \pm 0.13} \times 10^{14} \mathrm{M}_\odot\,. (8)$$

In order to apply this relation, we need to passively evolve the BCG to $z = 0.25$ and then evaluate its r-band luminosity ($M_\odot^r = 4.76$) yielding $L_{\mathrm{BCG}}^r \simeq 1.7 \times 10^{11}$ L$_\odot$. From Equ. 8 we obtain the mass estimate $M_{200} \simeq (2.4 \pm 0.4) \times 10^{14}M_\odot$ (ME 7a).

So far, we assumed that the BCG's stellar population is passively dimming without a change in stellar mass. If we instead assume a non-evolving absolute magnitude, i.e. the dimming of stellar light is compensated by stellar mass acquisition, then the r-band luminosity at $z = 0.25$ is 70% higher ($L_{\mathrm{BCG}}^r \simeq 2.9 \times 10^{11}$ L$_\odot$) resulting in a mass estimate of $M_{200} \simeq (4.4 \pm 0.7) \times 10^{14}M_\odot$ (ME 7b). For consistency with Reyes et al. (2008), we use the non-evolving luminosity as reference mass proxy, and treat the offset to the result including passive evolution as a systematic error. With an additional $\pm 10\%$ systematic for the SSP model evolution uncertainty and $\pm 20\%$ for the intrinsic scatter, we arrive at the final cluster mass estimate of $M_{200}^{L_{\mathrm{BCG}}} \simeq (4.4 \pm 0.7(^{+1.0}_{-2.2})) \times 10^{14}M_\odot$ (ME 7).

3.2.3. Optical luminosity

The next optical observable and useful mass proxy is the cluster luminosity L_{200}, defined as the summed r-band luminosity of all red ridgeline galaxies in N_{200}, K-corrected to $z = 0.25$ (Reyes et al. 2008). Following the procedures of the last two Sects. 3.2.1

and 3.2.2, we derive a total ridgeline z-band luminosity inside R_{200}^* of $L_{200}^z \simeq 9.2 \times 10^{12}\,L_\odot$ corresponding to $15.1 \cdot L_{\mathrm{BCG}}^z$. In contrast to the BCG, where the accretion of additional stellar mass can potentially compensate the dimming of its predominantly passive stellar population, the natural choice for the treatment of the total ridgeline light, which should be closely linked to the total stellar mass in the cluster, is the assumption of passively evolving luminosities. The expected evolved and transformed bulk luminosity in the r-band at $z = 0.25$ is therefore $L_{200}^r \simeq 2.5 \times 10^{12}\,L_\odot$. The corresponding scaling relation (in units of $h_{70}^{-2}\,L_\odot$ and $h_{70}^{-1}\,M_\odot$)

$$M_{200}^{L200} = f_{\mathrm{cr}}^{\mathrm{mean}}(2.51 \pm 0.24)\left(\frac{L_{200}^r}{8.16 \times 10^{11}L_\odot}\right)^{1.40 \pm 0.19} \times 10^{14} M_\odot \quad (9)$$

yields a total cluster mass estimate of $M_{200} \simeq (11.1 \pm 2.8) \times 10^{14} M_\odot$ (ME 8a). The systematic uncertainties now add up to about $\pm 34\%$, based on the discussed contributions from aperture rescaling (15%), color cut selection (20%), the SSP evolution model (10%), and the intrinsic scatter assumption (20%). The final L_{200} mass proxy for the cluster is hence $M_{200}^{L200} \simeq (11.1 \pm 2.8\,(\pm 3.7)) \times 10^{14} M_\odot$ (ME 8).

While the passively evolved BCG luminosity pointed towards a low cluster mass estimate (ME 7a), the total L_{200} light (ME 8) would give rise to the opposite conclusion of an extremely high total mass. This discrepancy is to be attributed to the highly populated bright end of the red galaxy ridgeline (see Fig. 2), which apparently places XMMU J1230.3+1339 in a low mass-to-light ratio regime (see Sect. 3.2.5) with respect to the underlying MaxBCG cluster sample used for the calibration of the L_{200} relation.

3.2.4. Optimal optical mass tracer

Reyes et al. (2008) also tested the possibility of an improved optical mass tracer by considering power law combinations of either the richness N_{200} or the total luminosity L_{200} with the BCG luminosity L_{BCG}. The resulting optimal optical mass tracer with an improved scatter of the form (in units of $h_{70}^{-2}\,L_\odot$ and $h_{70}^{-1}\,M_\odot$)

$$M_{200}^{\mathrm{opt}} = f_{\mathrm{cr}}^{\mathrm{mean}}(1.81 \pm 0.11)\left(\frac{N_{200}}{20}\right)^{1.20 \pm 0.09} \quad (10)$$

$$\cdot \left(\frac{L_{\mathrm{BCG}}}{\bar{L}_{\mathrm{BCG}}(N_{200})}\right)^{0.71 \pm 0.14} \times 10^{14} M_\odot$$

points towards an anti-correlation of the richness with the BCG luminosity at fixed cluster mass. Here $\bar{L}_{\mathrm{BCG}}(N_{200})$ is the mean local BCG luminosity at a given richness $\bar{L}_{\mathrm{BCG}}(N_{200}) = 3.14 \cdot N_{200}^{0.41} \times 10^{10} L_\odot$. Using the determined parameters for XMMU J1230.3+1339 with the non-evolved BCG luminosity $L_{\mathrm{BCG}}^r \simeq 2.9 \times 10^{11}\,L_\odot$ and $N_{200} \simeq 57$ we obtain an optimal optical mass estimate of $M_{200}^{\mathrm{opt}} = (8.6 \pm 1.3\,(^{+2.8}_{-3.9})) \times 10^{14} M_\odot$ (ME 9). The systematic uncertainties here include the richness systematics of Sect. 3.2.1 and the passive evolution offset discussed in Sect. 3.2.2, which would decrease the total mass by 32%.

3.2.5. Mass-to-light ratio

With our available LBT wide-field imaging data, we have an independent way to confirm the high optical luminosity of the cluster using the statistical background subtraction method. This approach does not include a color cut, i.e. also galaxies outside the red ridgeline region are counted in a statistical sense. We focus here on the uncontaminated R_{500} region of the cluster and determine the background luminosity in the 17 external regions as in Sect. 3.2.1, taking all galaxies with $m \geq m_{\mathrm{BCG}}$ into account. This way we measure a total background subtracted apparent z'-band magnitude of $m_{500,\mathrm{ap}}^{\mathrm{tot},z'} = 16.79$ mag within the R_{500} aperture, corresponding to a restframe luminosity of $L_{500,\mathrm{ap}}^{\mathrm{tot},z'} = (1.06 \pm 0.16) \times 10^{13} L_\odot$ (see Sect. 3.2.2). The integrated apparent magnitude of the cluster is comparable to the total foreground/background light contribution, implying that about half of all detected z'-band photons in the R_{500} region originate from XMMU J1230.3+1339. Only about 6% of this luminosity is contributed by faint galaxies with magnitudes $m^{z'} > 22.9$. The red ridgeline galaxies of Sect. 3.2.3 account for approximately 61% of the galaxy light with $m^{z'} \leq 22.9$ in the R_{500} region.

Although the system is at $z \sim 1$, the contrast of the cluster's z'-band light with respect to the integrated background is sufficiently high to allow an evaluation of the spatial light distribution in the core region and some surrounding substructures without any particular pre-selection of member galaxies. As before, we merely mask out stars and galaxies brighter than the BCG ($m < m_{\mathrm{BCG}}$) in the sky-subtracted z'-band image and apply Gaussian smoothing with a 180 kpc (22'') kernel over the field. The resulting observed z'-band light distribution of the cluster field is shown in the lower left panel of Fig. 9, displayed with 6 linear spaced contours corresponding to significance levels of 2σ-12σ above the background.

Next, we can derive the total z'-band mass-to-light ratio within the R_{500} aperture using the final best mass estimate of the cluster (see Sect. 5.2)

$$\left(\frac{M}{L^{z'}}\right)_{500,\mathrm{ap}} \simeq \frac{f_{3d \to \mathrm{ap}} \cdot M_{200}^{\mathrm{best}}}{f_{500 \to 200} \cdot L_{500,\mathrm{ap}}^{\mathrm{tot},z'}} = (46.7 \pm 11.3)\frac{M_\odot}{L_\odot}. \quad (11)$$

Here $f_{3d \to \mathrm{ap}} = M_{500,\mathrm{ap}}/M_{500} \simeq 1.65$ is the ratio of the aperture mass $M_{500,\mathrm{ap}}$ within a cylinder with radius R_{500} and the three dimensional spherically enclosed mass M_{500}, following the projection formula provided in Jee et al. (2005) for the derived single β-model parameters of the cluster. In order to compare this rather small value with locally determined mass-to-light ratios of clusters, we have to take evolution effects into account, since the optical luminosity is expected to undergo significant changes over a time span of 7.6 Gyr due to the increasing mean age of the underlying stellar populations. A suitable approximation for this change in the integrated luminosity is the passive evolution model, since the total light is dominated by galaxies on the red ridgeline or very close to it in color space. This model predicts a dimming of the absolute z'-magnitude by 0.7 mag, equivalent to a decrease of the luminosity by a factor of 1.9 at $z = 0$, resulting in an evolved mass-to-light-ratio of $(M/L^{z'})_{500,\mathrm{ap}}^{z=0} \simeq 89\,(M_\odot/L_\odot)$. The transformation into the V-band leads to an additional increase to $(M/L^V)_{500,\mathrm{ap}}^{z=0} \simeq 184\,(M_\odot/L_\odot)$, i.e. to a mass-to-light ratio in the lower half of the M/L parameter region spanned by other massive local clusters (see e.g. Popesso et al. 2007).

3.2.6. Velocity dispersion

Under the assumption of virial equilibrium a dynamical mass estimate can be obtained from a measurement of the cluster's

radial velocity dispersion σ_r (e.g. Finn et al. 2005; Kurk et al. 2009)

$$M_{200} \simeq \frac{3\,\sigma_r^2\,R_{200}}{G} \simeq \frac{1.7}{E(z)} \left(\frac{\sigma_r}{1000\,\mathrm{km\,s^{-1}}} \right)^3 \times 10^{15}\,h_{70}^{-1}\,\mathrm{M_\odot}\;. \quad (12)$$

We determined the velocity dispersion for XMMU J1230.3+1339 using the 'robust' estimator of Beers et al. (1990) and Girardi et al. (1993) applied to the 13 secure cluster members[12] in Table 2 and found $\sigma_r \simeq 658 \pm 277\,\mathrm{km\,s^{-1}}$ (Fig. 5) in good agreement with the classical dispersion measure of Danese et al. (1980). From Equ. 12 we derive a formal dynamical cluster mass estimate of $M_{200}^{\sigma_r} \simeq 2.8^{+5.2}_{-2.3} \times 10^{14}\,\mathrm{M_\odot}$ (ME 10).

Although the statistics of available galaxy member redshifts is low with corresponding large uncertainties, the general situation for a first dynamical mass estimate based on about a dozen redshifts is typical for most optical/infrared selected distant galaxy clusters (e.g. Stanford et al. 2005; Eisenhardt et al. 2008; Wilson et al. 2009; Muzzin et al. 2009). While at local redshifts dynamical mass estimators can provide robust measurements for relaxed clusters even for rather small spectroscopic samples (e.g. Biviano et al. 2006), high redshift systems are particularly prone to be affected by potentially significant biases. In the case of XMMU J1230.3+1339 the fairly low velocity dispersion estimate compared to similarly rich and massive local clusters becomes plausible in the light of the large-scale structure and component analysis in Sect. 4.2. More than half of the available redshifts are likely to be attributed to galaxies residing in coherently infalling structures, i.e. they are not virialized tracer particles of the underlying potential well. What is effectively measured is hence a combination of the 'fingers-of-God effect', corresponding to the virialized tracer particles the mass estimate is based upon, and the prolate ellipsoid in redshift space due to the coherent infall of the surrounding large-scale structure (e.g. Guzzo et al. 2008). The effect of this latter systematic velocity dispersion bias depends on the angle of the targeted bulk matter flows with respect to the plane of the sky, which can suppress the measured velocity dispersion in the case of coherently infalling substructures mainly in the transversal direction (see Fig. 12), or boost up the dynamical mass estimates for radial coherent flows.

3.2.7. Spatial galaxy distribution

As the final optical result discussed in this work we derive a spatial density map of the red ridgeline galaxies selected with the previously applied R−z color cut as shown in Fig. 2. The density map was constructed by marking the world coordinate positions of the 88 selected galaxies over the FORS 2 field-of-view and the subsequent application of an adaptive smoothing filter. The resulting spatial red ridgeline galaxy distribution is displayed in the upper left panel of Fig. 9 with log spaced color cuts and contour levels analogous to the representation of the X-ray surface brightness in the upper right panel. Going from the lowest to the highest contour level corresponds to a galaxy density increase by a factor of 26, with the peak density coinciding with the X-ray center marked by the white cross. Within the R_{500} region of the cluster, two additional galaxy concentrations towards the

North-West and South-East from the center are obvious. Along the same axis, galaxy overdensities can be traced out to beyond the nominal cluster radius. These components and features will be further discussed in the multi-wavelength view of the cluster in Sect. 4.

3.3. Weak lensing results

The projected total mass surface density is observationally accessible through the method of weak gravitational lensing. We have used the deep multi-band LBT imaging data of Sect. 2.1.2 to perform a full weak lensing analysis in the field of XMMU J1230.3+1339, which is presented in detail in the accompanying Paper II. For obtaining a complete multi-wavelength view on the cluster, we summarize here some relevant results of the analysis for this work.

With a redshift of $z \sim 1$, XMMU J1230.3+1339 is currently at the feasibility limit for weak lensing studies using ground-based imaging data. However, the available LBT data allowed the detection of a significant weak lensing signal based on the shape distortions of background galaxies, which were separated from foreground objects by means of multi-band photometric redshifts. The resulting weak lensing signal-to-noise map, which is proportional to the projected total mass surface density, is displayed in the lower right panel of Fig. 9. The five linearly spaced contour levels span the significance range from half the peak value ($1.75\,\sigma$) to the maximum at $3.5\,\sigma$. The location of this mass density maximum coincides with the X-ray center and the peak of the galaxy overdensity. Furthermore, the general cluster elongation in the SE-NW direction is also clearly visible in the weak lensing map. The detected extension towards the North-West is significant to better than $2\,\sigma$, whereas the South-Western feature is to be considered tentatively due to the close proximity to the contaminating foreground galaxy NGC 4477.

For the reconstruction of the total spherical 3D-mass of the cluster we fitted two parametric mass models to the observed tangential shear profile (see Paper II for details). For an assumed singular isothermal sphere (SIS) density profile we determine the corresponding best fitting velocity dispersion of the cluster to be $\sigma_r^{\mathrm{SIS}} \simeq 1271 \pm 255\,\mathrm{km\,s^{-1}}$. Using R_{200} of Sect. 3.1.1 as outer cluster boundary we obtain a SIS model[13] mass estimate (ME 11) of

$$M_{200}^{\mathrm{SIS}} \simeq 4.65 \cdot \left(\frac{\sigma_r^{\mathrm{SIS}}}{1000\,\mathrm{km\,s^{-1}}} \right)^2 \left(\frac{R_{200}}{1\,\mathrm{Mpc}} \right) \times 10^{14}\,\mathrm{M_\odot} \quad (13)$$

$$\simeq (7.6 \pm 3.3\,(+3.0)) \times 10^{14}\,\mathrm{M_\odot}\;.$$

As a second parametric model we considered a Navarro-Frenk-White (NFW) density profile (Navarro et al. 1997) with a concentration parameter of $c = 4.0$ and a scale radius of $r_s = 354\,\mathrm{kpc}$[14]. These NFW parameters were determined from the measured shear components, in good agreement with the expected values from simulations of halos of similar mass and redshift by Bullock et al. (2001) and Dolag et al. (2004). This best fit NFW model to the weak lensing data yields an enclosed total mass within R_{200} of $M_{200}^{\mathrm{NFW}} \simeq (6.9 \pm 3.3\,(+2.2)) \times 10^{14}\,\mathrm{M_\odot}$ (ME 12).

For consistency and robustness we used the X-ray determined value for R_{200} as outer cluster boundary. However, this way the weak lensing mass estimate is not fully independent.

---

[12] This method yields a slightly lower estimated cluster redshift of $z_{\mathrm{cl}} = 0.9737$ compared to the median redshift $\bar{z} = 0.9745$ of Sect. 2.1.3, but still well within the $1\,\sigma$ uncertainty. The first value is likely biased low due to coherently infalling sub-structure (see Sect. 4.2.1), so that the median value is preferable as cluster-centric reference point.

[13] Based on a fit to 10 data points out to $10'$.

[14] For h_{70}, slightly scaled from the values given in Paper II for h_{72}.
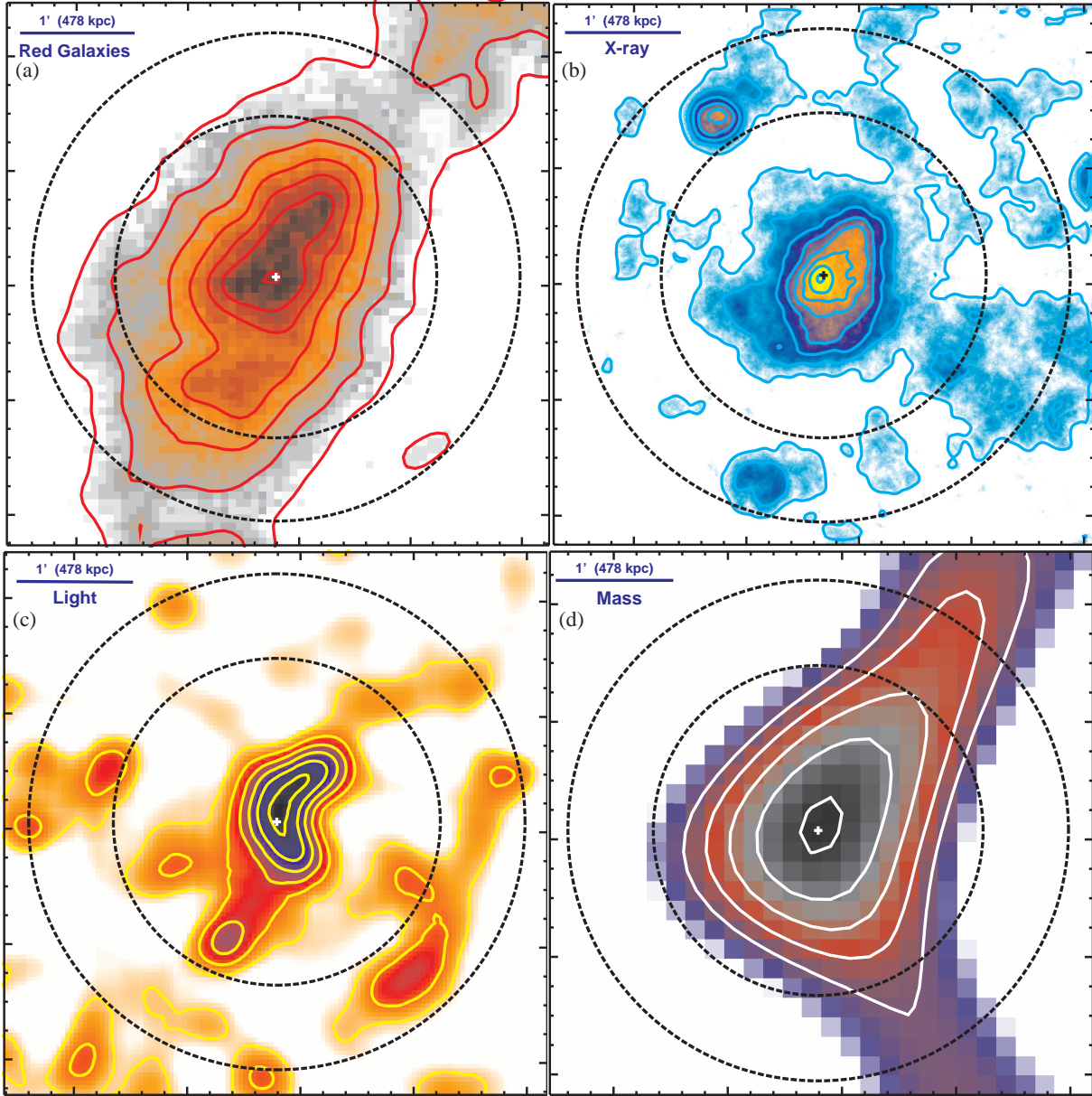
Fig. 9. A pan-chromatic view of XMMU J1230.3+1339 seen through projected surface density maps of different physical quantities within the cluster's R_{200} region (outer dashed circle). All panels show the same $4.8' \times 4.8'$ sky region in standard orientation (North is up, East to left), the nominal cluster center (central cross) and R_{500} (inner dashed circle) are also indicated. *Top left (a):* Density map of color-selected red galaxies (log-spaced contours). *Top right (b): Chandra* X-ray surface brightness map (log-spaced contours). *Bottom left (c):* Total z'-band light distribution map (linearly-spaced contours). *Bottom right (d):* Weak lensing mass density map (linearly-spaced contours).

Indeed, the self-consistent direct determination of R_{200} from the best fitting NFW profile yields a significantly larger radius of $R_{200}^{\mathrm{NFW}} \simeq 1415\,\mathrm{kpc}$. To account for this potential positive offset in the outer cluster radius, we considered the resulting mass differences as additional systematic uncertainty.

4. Multi-wavelength view on large-scale structure and small-scale physics

We now combine the results derived for the different cluster components (i.e. galaxies, ICM, and Dark Matter) in order to obtain a detailed pan-chromatic view of XMMU J1230.3+1339.

4.1. Comparison of projected density maps

Figure 9 displays the four derived spatial density maps (Sect. 3) within the cluster's R_{200} region (outer dashed circle), corresponding to an angular image side length of $4.8'$. The maps are based on independent data sets or techniques and visualize different physical projected properties and matter components. The top panels show the log-spaced density contours of the red ridgeline galaxies (left, a), based on the VLT/FORS 2 data of Sect. 2.1.1, and the *Chandra* observed (Sect. 2.2.2) X-ray surface brightness distribution (right, b). The bottom panels display the linearly-spaced contours of the total projected light distribution in the z'-band (Sect. 3.2.5) on the left (c) and the weak lensing signal (Sect. 3.3) on the right (d) both derived from the deep LBT/LBC imaging data of Sect. 2.1.2 (see Paper II for details). In terms of physical projected cluster quantities, the WL signal
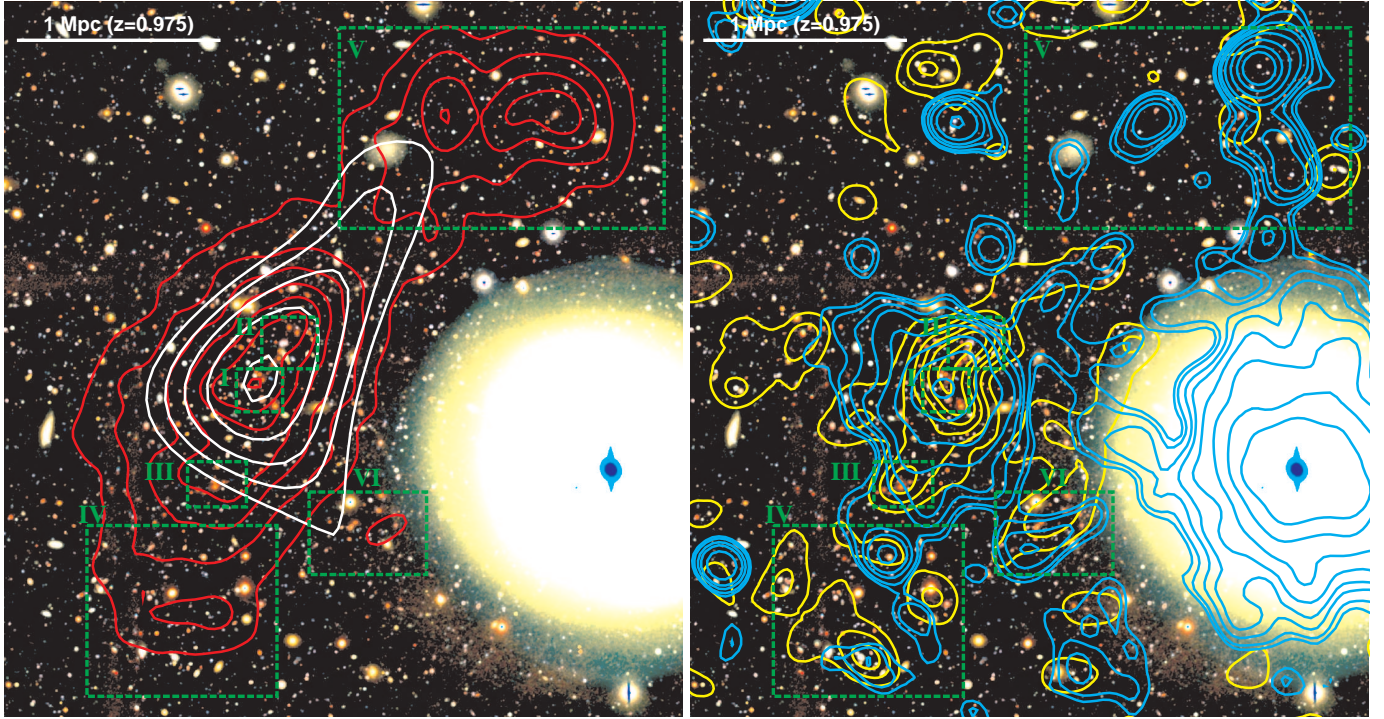
Fig. 10. Cluster components and large-scale structure environment of XMMU J1230.3+1339 in a $7.0' \times 7.3'$ LBT color composite view with different density contours overlaid. Six identified cluster components are marked by dashed green boxes labelled with roman numerals. *Left:* Contours show the galaxy densities in red and the weak lensing total mass density in white. *Right:* Same field with the z'-band light distribution in yellow and XMM-*Newton* X-ray contours in cyan.

is proportional to the total mass surface density (d), the observed z'-band flux represents the restframe B/V total stellar light (c), the X-ray surface brightness is a measure of the projected gas density squared n_e^2 (b), and the galaxies can be approximately considered as tracer particles of the underlying gravitational potential well (a).

The first observation is that the nominal cluster center (central cross), measured as the 'center-of-mass' of the X-ray emission detected with XMM-*Newton* (Sect. 3.1), shows a very good correspondence to the peak signal within a few arcseconds in all projected density maps. This implies that the galaxies, the ICM gas, and the dark matter component are linked to the same (projected) center of their corresponding density profiles. Note that this concordant cluster center for XMMU J1230.3+1339 does *not* coincide with the BCG location (see lower left panel of Fig. 1), which is often used as fiducial reference center in optical cluster studies.

A second common feature in all maps is an elongation or extension in the SE-NW direction, which indicates the apparent main axis for the cluster assembly and the connection to the large-scale structure filaments of the surrounding cosmic web. Just NW of the center, all projected density maps (at lower resolution for the WL signal) show another clear extension feature in the core region, which is identified with an ongoing merging event discussed in Sects. 4.2&4.4. The galaxy (a) and total matter overdensities (d) in the NW direction can even be traced to beyond the nominal R_{200} cluster radius, indicative for the presence of a LSS filament. In the opposite SE direction, the galaxy map (a) reveals a further density peak just inside the inner R_{500} radius, also reflected in the light map (c), and another extension to beyond the cluster radius.

Towards the South-Western (SW) direction from the system center, an additional but less pronounced likely cluster feature is

present in all maps. In contrast to the conclusions on the overall shape of XMMU J1230.3+1339 along the identified main NW-SE axis, which was not not influenced by NGC 4477 (see Fig. 10), the proximity to the bright foreground galaxy in the SW region now hinders the component analysis of the cluster in the far background and weakens the significance due to the deteriorated achievable shape and color measurement accuracy of background galaxies and possible residual contributions to the total light and X-ray emission in this region. As a result, the measured South-Western red galaxy density is to be regarded as lower limit (a), while the X-ray emission (b, see also the deeper XMM SNR map in Fig. 10, right) and total light distribution (c) could be slightly increased, and a tentative character applies to the SW feature in the weak lensing map (d).

4.2. Cluster components and large-scale structure

We turn the focus on the global view and the characterization of the dynamical state of XMMU J1230.3+1339 based on the available multi-wavelength data set. Figure 10 displays an optical color composite with a larger $7.0' \times 7.3'$ field-of-view and the different projected density contours overlaid. The weak lensing signal (white) and the galaxy densities (red) are shown in the left panel, and the z'-band light distribution (yellow) and the XMM-*Newton* X-ray emission (cyan) on the right. For a better qualitative evaluation of low surface brightness X-ray emission in the cluster outskirts the combined XMM-*Newton* data is used (Sect. 2.2.1) resulting in an improved sensitivity at the cost of lower spatial resolution compared to *Chandra*. The lowest four cyan contours correspond to significance levels of the X-ray emission of $(0.5, 1, 2, 3)\,\sigma$ above the background, whereas the central cluster contour displays a $35\,\sigma$ significance.

We have identified a total of six different cluster components or associated structures in the multi-wavelength maps, with identification labels I-VI in order of decreasing significance: the cluster core (I), an ongoing merger event towards the NW of the center (II), two infalling groups on the cluster outskirts (III & VI), and two filament extensions beyond the nominal cluster radius towards the South-East (IV) and the North-West (V).

The central cluster region, indicated by box I in Fig. 10, encompasses the projected density peaks of all the main matter components, i.e. the Dark Matter dominated total mass density (white contours), the hot ICM gas component (cyan), and the cold baryon component in form of the total stellar light (yellow) or the spatial galaxy density (red). The region also includes the spectroscopically confirmed BCG (ID 02 in Table 2) at a radial distance of $18''$ from the nominal cluster center (bottom panels of Fig. 1). For the further discussion, we follow the flow of accreted matter onto the main cluster halo from the largest scales towards the central regions.

Fig. 11. Closeup view on the infalling BCG2 group (III).

4.2.1. Cosmic web filaments

The North-Western galaxy filament (box V) is traced to a radial distance of more than twice R_{200}, where the current limit is set by the FORS 2 FoV, i.e. the actual overdensity of red galaxies might extend even further. The projected galaxy density appears to have a minimum close to R_{200} and then increases again towards the local maximum in the filament of region (V) (left panel of Fig. 10). Three spectroscopic cluster members (IDs 09,10,12 in Table 2) are located in the cluster-filament transition zone, all are blue shifted with respect to the median redshift with cluster-centric velocities in the range [-800,-1 300] km/s, which is indicative for a line-of-sight bulk flow velocity of the filament structure of $\simeq -1\,000$ km/s. In terms of the weak lensing mass density, the signal of an extended mass distribution is measured well into the cluster-filament transition regime at a signal-to-noise level of more than two. From the X-ray side, there are some indications for low surface brightness extensions from the cluster core towards the NW filament (right panel of Fig. 10), and several X-ray point sources in box V, which may or may not be related to the cluster environment.

The opposite galaxy extension towards the South-East (IV) is less pronounced and reaches about 0.5 Mpc beyond R_{200}. The association of the three X-ray sources with corresponding light overdensities in box IV to the filament can currently not be probed with the limited spectroscopy available, which includes one secure member galaxy (ID 11 in Table 2) matching the median redshift, i.e. with vanishing cluster-centric line-of-sight velocity. The tentative interpretation of a galaxy filament along the plane of the sky is fostered by the similar cluster-centric velocity of BCG2 (ID 08) as part of the infalling galaxy group III just inside R_{500}.

4.2.2. Infalling groups on the cluster outskirts

BCG2 (see Sect. 3.2.2) appears to be the central galaxy of an intact group environment approaching the cluster center from the SE. Figure 11 displays a closeup view on this group component (III), which still seems to be a bound sub-system without signs of strong interactions with the main cluster components yet. The very low cluster-centric velocity of BCG2 points at a radial infall orbit towards the center of XMMU J1230.3+1339 along the plane of the sky with a current cluster-centric distance of about 560 kpc. The BCG2 group is clearly visible as a local peak in
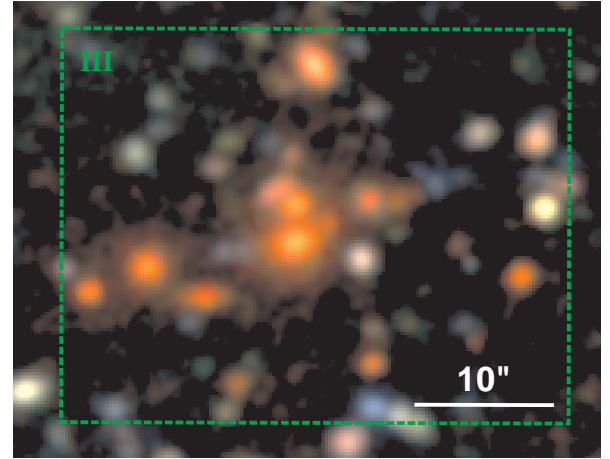
the red galaxy density (a) or total light (c) map of Fig. 9 and a less pronounced distortion in the XMM-*Newton* X-ray contours (right panel of Fig. 10). At the current mass and spatial resolution of the weak lensing map, the BCG2 group does not produce a local mass peak feature in the weak lensing contours, suggesting that the associated total mass of the BCG2 group is small compared to the main cluster halo.

A second infalling group candidate at a slightly larger projected cluster-centric distance of about 900 kpc is marked as component VI in Fig. 10. This South-Western cluster component is currently the least secure one, as spectroscopic confirmation is still lacking and the discussed proximity to NGC 4477 may impose a bias on the projected quantities. Nevertheless, all four density maps show features that point towards an off-axis infall scenario of matter also from the SW direction, but currently unconstrained along the radial direction. Besides the tentative mass feature in the weak lensing map (white contours) in the direction of component VI, XMM-*Newton* detects X-ray emission within this region on the 3σ significance level (cyan). This X-ray emission seems to be extended, but due to the low-surface brightness a further characterization is currently not feasible. The general, almost tangential direction with respect to the cluster center is also outlined by the coincident total light distribution of this region (yellow) and the density of red galaxies (red), which is certainly biased low compared to the true density as a result of color contamination from the blue foreground emission on the outskirts of NGC 4477.

4.2.3. Central merging activity

Moving back into the core region of XMMU J1230.3+1339, we now turn to the cluster component II, which extends to the North-West of the nominal center at a projected cluster-centric distance of 100-400 kpc. This component features prominently in the galaxy density (a) and total light (c) maps of Fig. 9 as linear NW prolongation close to the central peak value. The *Chandra* X-ray surface brightness map (b) reveals an associated wedge-like region with an almost constant SB, followed by a rapid outward SB decline at a projected distance of about 250 kpc. This surface brightness plateau was already visible in the azimuthally averaged radial SB profile of Fig. 8 and can also be recognized at lower spatial resolution in the XMM-*Newton* X-ray contours of Fig. 10. The weak lensing map (d) provides a view on the total mass distribution at a further reduction of resolution, but

still reveals a significant elongation of the projected mass in the direction of component II.

The overall geometry and features in the projected density maps are similar to the merger configuration in the well studied 'Bullet Cluster' 1E 0657-56 at a lower redshift of $z \simeq 0.3$ (e.g. Markevitch et al. 2002; Clowe et al. 2006; Bradač et al. 2006). In comparison, the observable signs of merging activity in XMMU J1230.3+1339 occur at smaller angular scales of $\lesssim 1'$ and correspondingly shorter projected physical distances of $\lesssim 500$ kpc, which implies either a steeper viewing angle with respect to the plane-of-the sky or a merger event closer to cluster core passage.

All currently available redshifts within component II are blue-shifted with respect to the median zeropoint. Besides one secure member (ID 01 in Table 2) at cluster-centric line-of-sight velocity of $\simeq -400$ km/s, four more tentative redshifts were identified closer towards the NW front at larger blue-shifted values of about [-700,-1300,-1300,-2800] km/s, shown as squares in the lower left quadrant of Fig. 5. With the currently available spectroscopy, we can establish a negative line-of-sight bulk velocity of the central merger component II, with a tentative best estimate for the center-of-mass velocity of the merging group of $v_r \simeq (-800 \pm 500)$ km/s.

4.3. 3D mass accretion geometry

Using the identified cluster components in the 2D multi-wavelength maps of Sect. 4.2 and the available spectroscopic information, we can reconstruct a tentative model of the three-dimensional accretion geometry of the cluster environment of XMMU J1230.3+1339. In Fig. 12, the horizontal directions corresponds to a cut along the cluster's principal SE-NW axis, and the vertical direction indicates the tentatively identified radial line-of-sight configuration consistent with the currently available limited spectroscopic information for the individual components I-V. Component VI is not considered here since the orientation along the redshift space direction is not constrained at the moment.

The cluster core (component I) with the nominal center (cross) and the offset BCG (black dot) was most likely passed by the group bullet (II) within the last 100 Myr at a small but non-zero impact parameter under a relatively small angle with respect to the plane-of-the-sky (see Sect 4.4). Judging from the undistorted galaxies in the immediate vicinity of the nominal cluster center, and the concordant peak location in the density maps of the galaxy-, light-, ICM-, and total mass distribution, the indications do not support the scenario of a direct hit (i.e. zero impact parameter) of the seemingly intact cluster center. The green arrow connected to component II visualizes the approximate traversed distance of an assumed linearly extrapolated bullet trajectory at a relative group velocity of 2500 km/s within 200 Myr. This distance of $\simeq 0.5$ Mpc emphasizes the relatively short timescale of ~ 100 Myr of a fierce interaction of the cluster core with the infalling group, and the implied rarity of these events to be 'caught-in-the-act'.

The BCG2 group (component III) has recently entered the R_{500} region of the main cluster from the South-East and does not yet show visual signs of interactions with the main halo. The spectroscopic information indicates a radial orbit with a minimal impact parameter. Assuming a reasonable fiducial current infall velocity of 1000 km/s, we obtain a traversed distance of about 200 kpc in 200 Myr (green arrow), and a likely direct core impact within a timescale of roughly ~ 0.5 Gyr. For similar assumed fiducial bulk flow velocities (e.g. Pivato et al. 2006) from
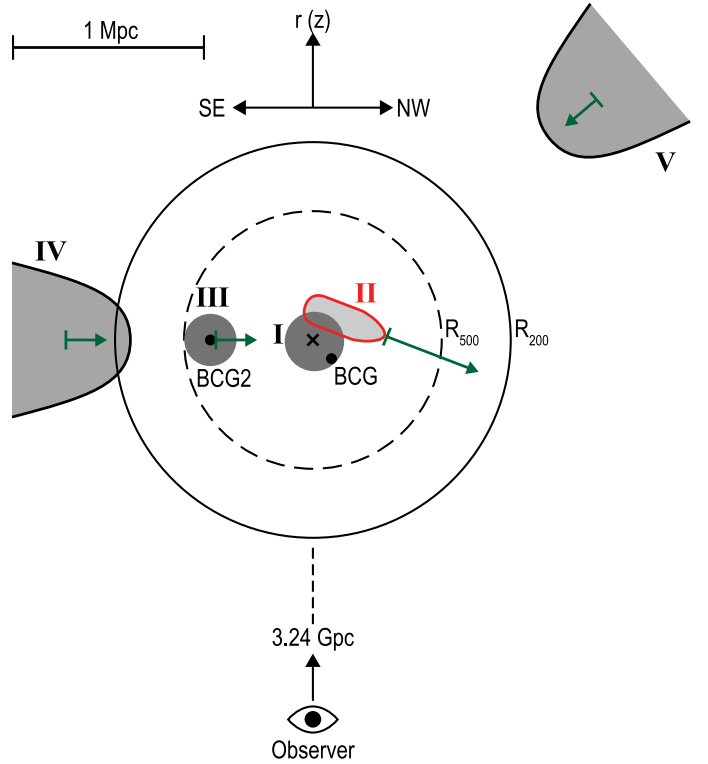
Fig. 12. Sketch of the reconstructed 3D accretion geometry for the cluster environment. The horizontal direction shows a cut through the main SE-NW cluster axis, whereas the tentative radial (i.e. redshift space) distances are plotted along the vertical axis for components I-V. The nominal cluster center is indicated by the central cross, the positions of the BCG and BCG2 by dots, and the reference radii R_{200} and R_{500} by the solid and dashed circles. The physical scale in the cluster reference frame is given in the upper left corner and the value in the lower part refers to the comoving distance to the cluster in the assumed cosmology. Green arrows indicate schematically the approximate traversed distance within 200 Myr for linearly extrapolated trajectories under the assumption of matter infall velocities of 2500 km/s for the central merging group II (see Sect. 4.4) and fiducial reference values of 1000 km/s for the outer components (III,IV,V).

the identified galaxy filaments IV and V, the timescales for matter infall to the cluster core are approximately 1-2 Gyr. From this first model of the 3D configuration of XMMU J1230.3+1339 and its large-scale structure environment, the cluster is likely to be in a continuing active mass accretion and growth phase for several Giga years to come.

4.4. The central group 'bullet'

Merging events constitute a crucial role in the galaxy cluster growth history within the hierarchical structure formation framework. However, the in situ capture of merging events close to the cluster core passage is rare due to the relatively short core interaction and crossing timescale of the order of 100 Myr. Since merger events are important laboratories for a rich number of further detailed investigations on Dark Matter properties, shock physics of the ICM, galaxy interactions and disruptions, and relativistic particle acceleration, we summarize the current observational status of the new high-z group 'bullet' in XMMU J1230.3+1339 here in order to establish a tentative multi-wavelength reference model of the merger configuration,

which is to be tested and extended with upcoming deeper observations.

Figure 13 shows the currently most detailed optical view on the dynamically active region of interest to the North-West of the nominal cluster center, with *Chandra* X-ray contours and the position of a VLA/FIRST radio source overlaid.

4.4.1. Merging features in the ICM

The merging process of a sub-cluster with the main halo is expected to occur at peak velocities corresponding to typical Mach numbers of $M = v/c_s \simeq 1\text{-}3$, where c_s is the velocity of sound in the main cluster and v is the relative velocity of the colliding gas fronts (e.g. Markevitch & Vikhlinin 2007). Interestingly, the expected typical value is obtained, when interpreting the opening angle with respect to the symmetry axis of the observed wedge-like structure in the X-ray surface brightness map as Mach cone. The dashed yellow lines in Fig. 13 represent the approximate observed wedges of constant surface brightness with an opening angle of $\varphi \simeq 28°$, which yields $M = 1/\sin(\varphi) \simeq 2.1$. The currently available *Chandra* data does not have sufficient depth for detailed diagnostics of the wedge-like X-ray surface brightness discontinuity, which would require measurements of the gas density and temperature jumps across the front. However, using this typical Mach number of $M \simeq 2.1$ as a first estimate for the relative velocities, we can obtain a first approximation of the orientation angle with respect to the plane of the sky. From the ICM temperature $T_X \simeq 5.3\,\text{keV} \simeq 6.2 \times 10^7\,\text{K}$ we derive a sound velocity of $c_s \simeq 1480 \cdot (T/10^8 \text{K})^{1/2}\,\text{km/s} \simeq 1160\,\text{km/s}$, and hence a relative velocity between merging group and cluster of $v_{\text{rel}} \simeq 2400\,\text{km/s}$. The combination with the radial line-of-sight velocity component estimate of $v_r \simeq -800\,\text{km/s}$ yields a first approximation for the angle of the merger axis with respect to the plane-of-the-sky of $\simeq 20°$.

In analogy to the 'Bullet Cluster' 1E 0657-56, the observed wedge structure in XMMU J1230.3+1339 is likely a 'cold front' in the 'stripping stage', i.e. a contact discontinuity on the boundary of the colder gas of the merging group and the hotter cluster ICM expected to form close to the core passage point (e.g. Markevitch & Vikhlinin 2007). The associated bow shock, as seen in 1E 0657-56, is expected to be detectable only on the outbound trajectory, i.e. it might not have formed prominently yet at the particular merger stage in XMMU J1230.3+1339. The tentative interpretation of a bullet-like merging event close to core passage with an observable 'cold front' (i.e. with an outward rising temperature) would also be consistent with the indications of an increasing ICM temperature at radii beyond the SB wedge (Sect. 2.2.1). Moreover, in the early 'stripping stages' the SB wedge opening angle could be closer connected to the actual Mach cone, which is not the case any more for cluster 1E 0657-56 due to the decreasing bullet size with time and a corresponding increase in the apparent opening angle (Markevitch & Vikhlinin 2007). A more detailed X-ray analysis of the merging physics in XMMU J1230.3+1339 based on deeper *Chandra* observations will be presented in a forthcoming paper.

4.4.2. Interactions of the galaxy component

Indications for seeing a snapshot of an early merger stage close to core passage also arise from a closer look at the galaxy component in Fig. 13. The front end of the X-ray wedge exhibits a surprisingly coincident alignment with a dense cloud of galaxies (upper right quarter of Fig. 13), seemingly the leading front of
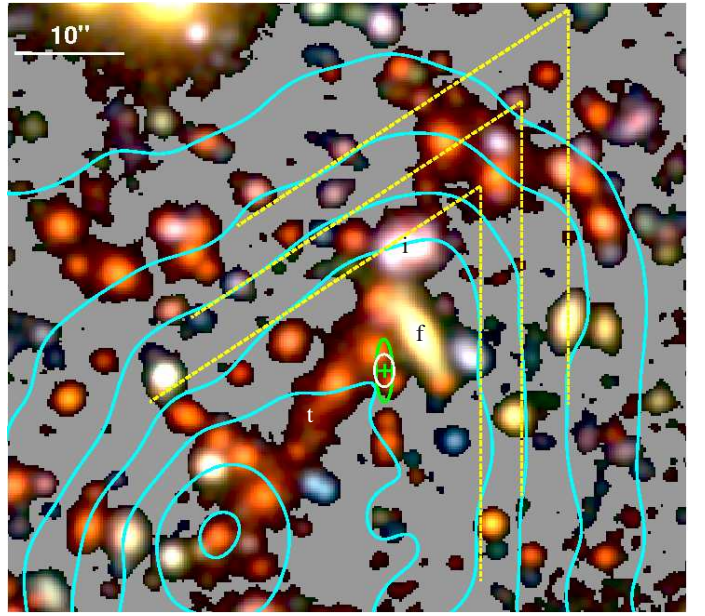
Fig. 13. Zoom on the dynamically active North-Western core region of the cluster. The 62″×55″ LBT/LBC optical color composite displays the Northern part of core component (I) and a full view on region (II) identified in Fig. 10. The *Chandra* X-ray surface brightness contours (cyan) exhibit a pronounced cone-like structure with an approximate opening angle of 56 deg (yellow lines). Marginally extended 1.4 GHz radio emission is detected along the approximate symmetry axis of the configuration, displayed by the green cross for the location, the white spatial error ellipse, and the green ellipse indicating the observed source shape and extent. Character labels refer to candidate events of tidal stripping (t), galaxy-galaxy interaction (i), and a foreground galaxy (f). To enhance the contrast of low surface brightness features in the optical image, a smoothing with a 0.7″ Gaussian kernel was applied to the data, and the black background was remapped to gray scale.

the merging group's galaxy content. The practically collisionless galaxy component has thus not yet been spatially separated from the fluid-like ICM component, as in the case of 1E 0657-56.

Several galaxies in the central part of Fig. 13 show signs of ongoing galaxy transformation processes. The object with the bright core (label i) at the inner tip of the wedge North of the yellow foreground spiral (label f) is a candidate event for the collision of two gas rich galaxies, based on the strong distortions of the inner isophotes and the blue color. The photometric redshift $z_{\text{phot}} \simeq 1.0$ of Paper II for this galaxy indicates a tentative cluster membership, which is to be spectroscopically confirmed. A different process is seen at work in the red spectroscopic cluster member (ID01 in Table 2) to the East of the green cross, which features a trail extending about 40 kpc to the SE (label t). This galaxy trail could be tidally stripped stellar material resulting from the gravitational interaction with the core of the main halo and could end up as part of the Intracluster Light (ICL) (e.g. Zibetti et al. 2005). More detailed studies on galaxies transformation processes in the dynamically active core region of XMMU J1230.3+1339 will require high-resolution space-based imaging and spectroscopic information for the individual objects.

4.4.3. Dark Matter halo properties

The elongation in the total projected mass distribution seen in the weak lensing map and the high galaxy density associated with the group bullet suggest that the initial mass of the merg-

ing group corresponds to a significant fraction of the main cluster. With the available ground-based WL data the group mass cannot be further constrained at the moment, but a reasonable assumption would be a bullet mass of the order of $10^{14}\,M_\odot$ corresponding approximately to a 1:4 merger scenario.

Hydrodynamical simulations to reproduce the observed properties of the merging system 1E 0657-56 by Springel & Farrar (2007) have shown that the time dependent spatial separation of the mass peak of the bullet group relative to the ICM and the shape of the contact discontinuity in the X-ray surface brightness depend sensitively on the relative concentrations of the merging halos and their gas fractions. A first visual comparison of the merger configuration in XMMU J1230.3+1339 to these simulations seem to be consistent with a low concentration parameter of $c \simeq 2$-3 for the main halo and a time snapshot within about 100 Myr of the closest core passage point.

4.4.4. Observed extended radio emission

An additional point of particular interest is the observation of extended radio emission originating from a location trailing the front of the infalling group very close to the approximate symmetry axis of the merger configuration. In Fig. 13, the location of the detected 1.4 GHz radio source (ID: J123016.1+133917) from the VLA FIRST survey (White et al. 1997; Becker et al. 2003) is indicated by the green cross in the center of the image. This source with a signal-to-noise ratio of 7.2 is the only catalog entry within the field of the larger cluster environment shown in Fig. 10. The radio source is clearly extended with good significance along the North-South axis with a deconvolved FWHM of $(5.7 \pm 1.5)''$, but below the extent detection threshold along the orthogonal East-West axis. The reconstructed source shape is indicated by the green ellipse in Fig. 13, where the upper $1\,\sigma$ limit of the extent along the minor axis of 1.5″ was used. The white ellipse displays the positional error region of the source center at 90% confidence, which is just small enough to exclude any of the centers of the neighboring galaxies as origin for the radio emission at this confidence level[15]. The 1.4 GHz radio source has an integrated flux of (1.69 ± 0.19) mJy, which translates into a total radio power of $P_{1440\,\mathrm{MHz}} \simeq 8.3 \times 10^{24}$ W Hz^{-1} at the cluster redshift under the assumption of a typical spectral index of -1 for the extended emission (e.g. Laing & Peacock 1980).

4.4.5. What is the origin of the radio emission?

The simplest explanation for the observed radio emission close to the core region of XMMU J1230.3+1339 would be an extended radio lobe associated with central AGN activity in one of the cores of the two red early-type galaxies partially encompassed by the white positional error ellipse in Fig. 13. In fact, Dunn et al. (2010) have found extended radio emission in more than half of the early-type galaxies of a complete local sample of X-ray luminous E and S0 galaxies. However, only the two most radio luminous objects in this sample (M87 & NGC 4696) would have comparable radio powers to the source in XMMU J1230.3+1339, but these are associated with BCGs of local clusters. With the currently available radio data on the field, the association of the detected radio source with a nearby galaxy cannot be ruled out and is certainly a valid hypothesis.

However, the fact that we are most likely witnessing an ongoing merger event close to cluster core passage suggests the consideration and discussion of an alternative scenario on the basis of turbulence-induced electron acceleration in the wake of infalling substructure. This mechanism of turbulence (re)acceleration (e.g. Brunetti et al. 2001; Fujita et al. 2003; Brunetti et al. 2004) is now believed to be the source of relativistic electrons associated with the giant radio halos observed in a growing number of massive clusters with recent merger activity such as Coma (e.g. Feretti & Giovannini 2008; Ferrari et al. 2008, for reviews). The generation and time evolution of fluid turbulence behind a moving subcluster can be probed and visualized with numerical hydrodynamic simulations (e.g. Takizawa 2005; Dolag et al. 2008; Vazza et al. 2009). The overall geometry and involved length scales seen in such numerical studies are comparable to the observed configuration shown in Fig. 13, implying that merger-generated turbulence at the location of the observed radio emission in XMMU J1230.3+1339 is plausible and even expected.

An intriguing scenario would be that we are actually witnessing the injection point of re-accelerated ultra-relativistic electrons into the ICM as the source for the later development of a giant radio halo filling a good fraction of the cluster volume with low surface brightness radio emission. With the current radio data, we can only perform some consistency checks to test the plausibility of this alternative hypothesis.

Cassano et al. (2007) derived the expected scaling relations of the re-acceleration model for the total emitted radio power with total cluster mass and other properties, which is reflected in the observed strong empirical correlations. The latest radio power correlation measurements are provided by Brunetti et al. (2009) for the $P_{1440\,\mathrm{MHz}}$-$L_{\mathrm{X}}^{\mathrm{bol}}$ relation[16] yielding $\log(P_{1440\,\mathrm{MHz}}/\mathrm{W\,Hz}^{-1}) - 24.5 = (0.077 \pm 0.057) + (1.76 \pm 0.16)\,[\log(L_{\mathrm{X}}^{\mathrm{bol}}/\mathrm{erg\,s}^{-1}) - 45.4]$. The combination of this correlation with the non-evolving $L_{\mathrm{X,500}}^{\mathrm{bol}}$-$M_{500}$ relation (Equ. 4) results in

$$M_{200} \simeq f_{500\to200} \left(\frac{f_{\mathrm{tot}\to500}^{L_X}}{E^{\frac{4}{3}}(z)} \right)^{0.48} \left(\frac{P_{1440\,\mathrm{MHz}}}{8.6 \times 10^{24}\,\mathrm{W/Hz}} \right)^{0.27} \times 10^{15} M_\odot \,. \quad (14)$$

Here $f_{\mathrm{tot}\to500}^{L_X} \simeq 0.95$ is a conversion factor from total luminosity to $L_{\mathrm{X,500}}^{\mathrm{bol}}$ and $f_{500\to200} \simeq 1.4$ as defined in Sect. 3.1.1. Applying this relation to the measured radio power in XMMU J1230.3+1339, we obtain a mass estimate of $M_{200}^{1.4\,\mathrm{GHz}} \simeq (9.5 \pm 3.8) \times 10^{14}\,M_\odot$ (ME 13). The error is dominated by the systematic uncertainty in the redshift evolution of $L_{\mathrm{X,500}}^{\mathrm{bol}}$-$M_{500}$ (Sect. 3.1.3). Other error contributions such as the uncertainties for the total radio flux ($\pm12\%$), the K-correction from the assumed spectral index ($\pm20\%$), and the used scaling relations are added in quadrature.

This plausibility check for the hypothesis that the observed marginally extended radio emission is related to the origin of the radio halos in lower redshift clusters yields a mass in fairly good agreement with the best total mass estimate for XMMU J1230.3+1339. Turning the argument around implies that for the inferred total cluster mass the observed total radio power is just a factor of a few higher than expected for the total radio halo emission, which might be expected close to the core passage of a subcluster. Hence, the scenario of the turbulence-induced electron re-acceleration model connected to the ongoing merging activity seems also to be a consistent alternative

---

[15] The nearest previously known foreground galaxy (label f in Fig. 13) SDSS J123015.88+133920.4 has a spatial separation of 4.3″ from the radio source, corresponding to a distance of about a factor of 4 outside the 90% positional error ellipse of the FIRST source.

[16] Using the BCES Bisector parameters.

and should be further pursued. Considering that current detailed measurements of diffuse radio emission in clusters are limited to $z < 0.6$ (Brunetti et al. 2009), future low-frequency radio studies of the dynamically active core region of XMMU J1230.3+1339 have the potential to gain new insights into the origin and evolution of radio halos.

5. Discussion

In the following section we discuss the dynamical state of the system and evaluate the different mass estimates and scaling relations used to derive them. We then compare XMMU J1230.3+1339 to other high-z galaxy clusters and focus on the connection to low redshift counterparts.

5.1. Dynamical state of XMMU J1230.3+1339

The system XMMU J1230.3+1339 is a massive bona fide cluster with ongoing dynamical activity on all relevant scales. We will argue in the following that this cluster, observed at a lookback time of 7.6 Gyr, is likely a precursor of the most massive non-cool-core clusters in the local Universe, similar to the Coma system.

In the optical, XMMU J1230.3+1339 (see Table 3) exhibits a galaxy population which is among the richest of all known $z > 0.9$ clusters. On the X-ray side, the ICM is found to be hot, with a high luminosity and a rather extended surface brightness profile, devoid of any detectable X-ray point source within R_{500}. Moreover, the high total mass of the system enables complementary system diagnostics using weak lensing measurements. The cluster center of XMMU J1230.3+1339 is well defined, which indicates a virialized core region prior to the onset of the observed central merging event. The projected density maps reveal the galaxy and total light peaks, the center of the total mass, and the X-ray surface brightness peak all within a few arcseconds of each other (Fig. 9).

The location of the Brightest Cluster Galaxy at a projected distance of 18″ or 140 kpc from this nominal center shows a significant spatial offset. Considering the dynamical friction timescale of a few Gigayears, spatial offsets of the BCG from the center of the main cluster halo are not surprising when observing systems in the first half of cosmic time. However, in the local Universe the BCG location with respect to the X-ray center is known to correlate strongly with the dynamical state of the cluster. Sanderson et al. (2009) have shown that a large projected BCG offset ($> 0.02 R_{500}$) implies on average a non-cool core host cluster with a shallow central ICM gas density profile, a larger than average gas mass fraction, and very low star formation and AGN activity associated with the BCG itself. These local ($z \sim 0.2$) correlations and expectations for clusters with significant BCG offsets are tentatively consistent with the properties of XMMU J1230.3+1339, with the exception of the gas mass fraction, which is found to be close to the average local value (see Sect. 3.1.5).

The identified central merging event gives rise to a dynamically highly active central region of the cluster with various characteristic signatures as discussed in Sect. 4.4. Due to the quadratic dependence of thermal bremsstrahlung emissivity on the gas density, global ICM X-ray diagnostic measurements are expected to be influenced most by central group mergers. In the specific case of XMMU J1230.3+1339, the resulting flattening of the X-ray surface brightness within the wedge-like region in the wake of the infalling group is well visible in Fig. 9 (top right

panel). This feature is clearly a deviation from the underlying assumption of spherical symmetry and results effectively in a less reliable radial profile fit (Sect. 2.2.2) with an increased core radius r_c and slope parameter β with respect to the pre-merger configuration. Additionally, significant deviations from an assumed hydrostatic equilibrium state (Sect. 3.1) can be expected in the core region. The local ICM temperature could be lowered due to the cooler gas of the infalling group core, or temporarily boosted in the bow shock regions in conjunction with the X-ray luminosity. However, in the light of total cluster mass proxies of Sect. 5.2 this merging event does not seem to affect the results significantly. The interaction region is rather to be regarded as a localized perturbation with little influence on the still well defined cluster center and only mild effects on global quantities.

Standard cool core diagnostics classify XMMU-J1230.3+1339 in its current state as a Non-Cool-Core cluster (Sects. 2.2.2 & 3.1.4), albeit the relatively short central cooling time scale. Any possible previous onset for the development of a centrally peaked surface brightness profile was already flattened out by the group 'bullet' (component II). The foreseeable core impact of the BCG2 group (component III) will likely further disrupt the dense cluster center and hence erase the central conditions required for the progress of significant cooling. This scenario is consistent with the emerging picture from simulations on the different formation histories of NCC and CC clusters. The simulations of Burns et al. (2008) showed that Non-Cool-Core clusters are characterized by an increased mass accretion rate ($\gtrsim 50\%$ per Gyr) in early epochs ($z \gtrsim 0.8$), during which nascent cool cores are destroyed by major merger events which also set the conditions to prevent cooling at later epochs.

5.2. Comparison of mass estimates and scaling relations

In Sects. 3 & 4.4, we have derived a total of 13 different mass proxies for XMMU J1230.3+1339, which will be compared and discussed in the following.

5.2.1. Combined mass estimate

We have applied different and independent observational techniques to study and characterize the cluster based on (i) optical imaging data, (ii) X-ray observations, (iii) weak gravitational lensing, and (iv) spectroscopic information for a first glimpse on the system dynamics. The objective in this section is to combine several suitable measurements in order to obtain a (preliminary) best total mass estimate M_{200}^{best} as a benchmark value and starting point for a comparison of the different high-z mass proxies.

We start by selecting four reliable, quasi-independent mass estimates from different observational techniques as input for a combined mass estimate. On the X-ray side, the concordant *Chandra* and XMM-*Newton* ICM temperature estimate provides tight mass constraints based on the T_X-M (ME 1) scaling relation, which also encompasses a reliable redshift evolution prediction. The *Chandra* determined β-model SB structure parameters were the basis for the gas mass measurements of the system and the corresponding M_{200}^{gas} estimate (ME 4). This constitutes a second reliable and quasi-independent mass measurement, since the cooling function for the soft X-ray band is practically insensitive to the ICM temperature (few per cent changes over the relevant T_X range). Similarly, the temperature based R_{200} was chosen as cluster boundary for the weak lensing measurements, which was regarded as more robust compared to the self-consistent approach based on the current model constraints from
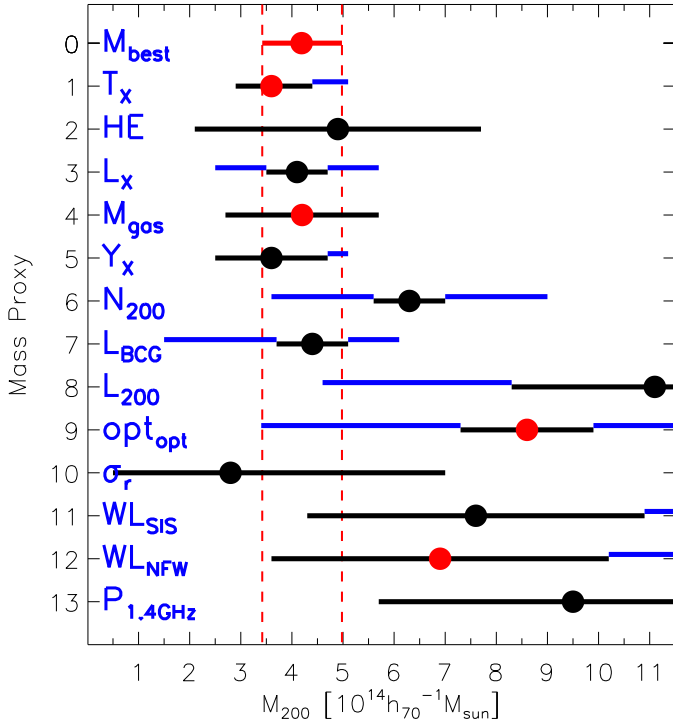
Fig. 14. Comparison of different mass proxies for cluster XMMU J1230.3+1339. The combined mass estimate $M_{200}^{best} \simeq 4.19_{-0.77}^{+0.79} \times 10^{14}$ M$_\odot$, shown on top with 1σ uncertainties (dashed lines), is based on the combination of four quasi independent mass proxies (red points). The numbering along the vertical axis is equivalent to the mass estimate labels (ME 1-13) in the text. Statistical 1σ uncertainties are shown by the black horizontal lines. The magnitude and direction of potential systematic offsets are displayed by the slightly shifted blue bars extending the statistical error for illustration purposes.

the ground-based weak lensing signal with larger uncertainties. We choose the NFW model estimate (ME 12) as WL input mass proxy for the M_{200}^{best} determination. As fourth reference mass, the 'optimal optical' mass tracer is considered (ME 9).

Besides the statistical uncertainties arising from measurement errors and the scatter in the used scaling relations, we also attempted to approximately quantify the influence of potential systematic offsets on the mass estimators. These latter uncertainties were due to e.g. smaller analysis apertures compared to the used scaling relations (T_X), the resulting influence on the derived cluster radii (WL), significant uncertainties in the redshift evolution (L_X, L_{BCG}, optical apertures), and technical ambiguities arising from the adaptation of local measurement recipes to high redshift (N_{200}, L_{200}). These technical uncertainties are in principle independent from the statistical errors, however, their (unknown) statistical occurrence may not follow a Gaussian probability distribution and are hence difficult to properly account for. As a first order approximation, we assume Gaussian properties of the systematic technical uncertainties and add them in quadrature to the statistical error intervals to obtain mass probability distributions for the individual proxies. The four[17] quasi-independent mass reference proxies are then combined with a maximum-likelihood approach, resulting in a final cluster mass estimate of $M_{200}^{best} = 4.19_{-0.77}^{+0.79} \times 10^{14}$ M$_\odot$ with specified 1σ un-

---

[17] The velocity dispersion-based dynamical mass estimate (ME 10) with the current uncertainty range has practically no statistical weight, its inclusion for the combined mass would only have a per cent effect.

certainties. This currently most likely total mass interval for XMMU J1230.3+1339 is shown in the mass proxy comparison plot in Fig. 14 (vertical dashed lines), together with the input reference proxies displayed by the red filled circles, and all other mass estimates (black circles) with their corresponding uncertainties.

5.2.2. Multi-wavelength mass proxies and challenges at high-z

The combined cluster mass proxy $M_{200}^{best} \simeq 4.2 \times 10^{14}$ M$_\odot$ with 1σ uncertainties of about 19% is currently the best reference value for XMMU J1230.3+1339 and is among the most accurate cluster masses measured to date at $z > 0.9$.

The X-ray derived mass estimates (ME 1-5) provide a consistent picture of the cluster with mostly well constrained mass intervals based on the medium deep *Chandra* and XMM-*Newton* data. The systematic uncertainties on T_X (ME 1) arise from the unconstrained temperature structure of the ICM and the possible influence of the central merging event. The constraints from the hydrostatic estimate (ME 2) are mostly limited by the uncertainties in the β-parameter, which is certainly influenced by the fly-through group bullet in addition to possible deviations from the hydrostatic assumption in the central regions. The uncertainties of the gas mass (ME 4) and Y_X (ME 5) estimates are mostly limited by the depth of the available X-ray data. The cluster property with the smallest relative uncertainty (see Table 3) is the X-ray luminosity L_X, which translates into small statistical mass estimate errors based on the latest (local) L_X-M scaling relation. However, a significant uncertainty is added because of the limited knowledge on the high-z evolution of the related L-T scaling relation (see Sect. 3.1.3). For the very good concordance of the L_X based mass estimate with M_{200}^{best}, the L_X-T relation was assumed to be non-evolving, which is different from the self-similar evolution expectations. However, such a breaking of self-similarity for the L_X-M scaling in terms of a slower redshift evolution and a steeper slope of the relation is in qualitatively good agreement with the latest results from the Millennium Gas Simulations after the inclusion of non-gravitational (pre-)heating mechanisms (Stanek et al. 2010). Once an improved and self-consistent calibration of the L_X scaling relations at $z > 0.9$ is available, the X-ray luminosity appears to have the potential to be a good high-z mass proxy at relatively low observational cost.

Weak lensing mass estimates are potentially a powerful tool to provide independent low-bias measurements to make progress in the calibration of mass-observable relations. However, the weak lensing analysis of XMMU J1230.3+1339 in Paper II is at the current feasibility limit for ground-based imaging observations, implying fairly large statistical uncertainties due to the limited lensing signal strength. M_{200}^{best} is on the lower mass end of the uncertainty range but still consistent within the errors with the WL mass proxies (ME 11 & 12). Significant progress and a self-consistent parameter treatment in the WL analysis will require the availability of deep spaced-based imaging data.

The dynamical cluster mass estimate based on the measured radial velocity dispersion σ_r (ME 10) provides the weakest statistical constraint for XMMU J1230.3+1339, due to the small dynamic range of σ_r and the relatively large uncertainties related to the limited number of available redshifts. The situation of having about a dozen spectroscopic cluster members for a first order evaluation of the velocity dispersion is typical under survey conditions with single mask spectroscopic follow-up of newly discovered high-z systems. More stringent mass constraints require large, dedicated follow-up programs to ideally increase the

number of cluster redshifts by an order of magnitude. Although hardly feasible in the general case for $z > 0.9$ clusters due to the magnitude limit of the available spectrographs, the high richness of XMMU J1230.3+1339 might realistically enable the identification of about 100 spectroscopic cluster members. However, biases arising from infalling structures, which could lead to positive and negative offsets depending on the line-of-sight angle, are likely to limit the achievable accuracy of dynamical mass estimates at high redshifts.

Mass proxies based on optical/NIR imaging data have the advantage of being observationally cheap and usually readily available for distant cluster searches or studies. Although significant progress has been made in the calibration of optical scaling relations at lower redshifts, unbiased mass proxies at $z > 0.9$ to better than 40-50% seem to require significant further work to overcome technical and evolutionary challenges. We have obtained a consistent picture that the optical galaxy population of XMMU J1230.3+1339 is rather remarkable for a high-z cluster, both in terms of total galaxy numbers (N_{200}, R^{rich}) and total luminosity (L_{200}, L_{500}^{tot}). Interestingly, the optical BCG luminosity (ME 7) yields a mass estimate which is fully consistent with M_{200}^{best}, followed by the suggested higher system masses of the N_{200} proxy (ME 6), the proposed optimal optical mass tracer (ME 9), and the L_{200} luminosity (ME 8). In the case of XMMU J1230.3+1339, the optimal optical mass tracer of Reyes et al. (2008) does not seem to improve the individual proxies based on N_{200} and L_{BCG}.

The use of luminosity-based mass proxies (e.g. L_{200}) at high-z requires as input rather large evolution and K-correction factors to relate them to the scaling relations calibrated at lower redshifts. Counting galaxies along the typically well-defined red-sequence of early-type galaxies (e.g. N_{200}) seems to be a more straightforward approach. However, even this apparently simple task gets increasingly complicated at high-z, where various subtleties and potential biases are to be taken into account if a somewhat reliable mass estimate is to be achieved. Even under the assumption that a distant cluster is sufficiently rich to exhibit an easily identifiable red-sequence, three main critical technical aspects remain and may impose significant mass biases: (i) finding the correct RS slope, (ii) the definition of appropriate color cuts, and (iii) the determination of a self-consistent measurement aperture. All three items are in principle functions of cluster redshift, and the first two depend moreover on the applied filter combination and the depth and quality of the data. As examples of redshift dependent biases, we can consider galaxy evolution effects in clusters, which lead to an observed increase with lookback time of the fraction of objects bluer than the red-sequence and also an increasing relative effective age (and hence color) difference of the average stellar populations as a function of cluster-centric radius (e.g. Rosati et al. 2009). For a fixed color cut definition, a redshift dependent positive or negative richness and mass bias could thus be imposed through an increasing contamination of bluer non-passive galaxies in the red ridgeline selection, or by excluding a growing fraction of slightly bluer passive galaxies on the cluster outskirts. Similar redshift dependent mass biases may arise through a non-consistent scaling of the measurement apertures.

An alternative approach applicable in the absence of a robust estimate for the cluster radius R_{200} or for direct cluster-to-cluster comparisons is to measure relevant cluster quantities inside a fixed physical projected radius of e.g. $1 \, h_{70}^{-1}$ Mpc. The hereby imposed positive mass bias with redshift might in many cases be an acceptable trade-off for otherwise large possible uncertainties in the cluster radius. In the case of XMMU J1230.3+1339, the ICM

temperature determined R_{200} is within 2% of $1 \, h_{70}^{-1}$ Mpc, implying effectively only percent level differences for most of the total mass estimates (ME 1-5, 7, 10-13), when re-scaled to the fixed physical aperture. However, for the optical mass proxies based on richness and total luminosity (ME 6, 8, 9) a significant reduction of the total mass estimate of the order of 30% applies for the fixed radius, which would move these proxies in much better agreement with the current best estimate M_{200}^{best}.

5.3. Comparison to similar X-ray clusters at $z \sim 1$

The growing number of known $z \sim 1$ galaxy clusters with available multi-wavelength data will soon allow comprehensive population studies from the group regime to the most massive systems at this important cosmic epoch. A point of particular interest will be the intrinsic cluster-to-cluster variations at a given epoch for systems with comparable masses, e.g. with respect to the thermodynamic properties of the ICM, the formation history of the galaxy population, or the structure of the Dark Matter halo. This intrinsic physical scatter sets on one hand the ultimate limit of accuracy for the calibration of high-z scaling relations and reflects on the other hand the different conditions during cluster formation, e.g. the collapse epoch, the influence of the LSS environment, or AGN feedback.

Within the XDCP survey, the cluster XMMU J1229.5+0151 at $z = 0.975$ (Santos et al. 2009) is almost the 'twin brother' of XMMU J1230.3+1339. Besides the concordant redshift, XMMU J1229.5+0151 features a comparable X-ray luminosity, a similar ICM temperature within the errors ($T_X \simeq 6.4$ keV), and a consistent velocity dispersion ($\sigma_r \simeq 683$ km/s). The cluster is also optically rich with a well populated red sequence and two bright galaxies in the center. A third bright galaxy of comparable magnitude and mass is located on the outskirts of the cluster, at a projected distance similar to the BCG2 group in XMMU J1230.3+1339. Overall, the basic global properties of the two clusters seem to be well consistent within the observational uncertainties.

The two most distant clusters from the Wide Angle ROSAT Pointed Survey (WARPS) (Perlman et al. 2002) are further appropriate candidates for a direct comparison with XMMU J1230.3+1339 as they are similar in mass and redshift. The most distant WARPS cluster, Cl 1415.1+3612 at $z = 1.03$, has an ICM temperature of $T_X \simeq 5.7$ keV, a luminosity of $L_{X,200}^{bol} \simeq 10.4 \times 10^{44}$ erg/s, a hydrostatic total mass estimate of $M_{200} \simeq 3.8 \times 10^{14} \, M_\odot$ (Maughan et al. 2006), and a velocity dispersion of $\sigma_r \simeq 810$ km/s (Huang et al. 2009). The second system Cl 1429.0+4241 at $z = 0.92$ is characterized by the parameters $T_X \simeq 6.2$ keV, $L_{X,200}^{bol} \simeq 9.6 \times 10^{44}$ erg/s, and $M_{200} \simeq 4.5 \times 10^{14} \, M_\odot$. With core radii of $r_c \sim 100$ kpc (for $\beta = 2/3$) both systems are more compact in their ICM structure compared to XMMU J1230.3+1339 and their bolometric X-ray luminosities are 40-50% higher, while the total mass and temperature estimates are similar within the uncertainties.

5.4. Appearance at $z = 0$

We now address the question of the expected system properties of XMMU J1230.3+1339 after an additional 7.6 Gyr of cluster evolution (i.e. $z = 0$) and compare these to the characteristics of the local Coma cluster ($z \simeq 0.023$).

A lower limit for the total system mass at $z = 0$, without considering further accretion, can be obtained from the self-similar evolution model. Due to the decreasing reference den-

sity $\rho_{cr}(z)$ with time, the system radius is expected to evolve as $R_{200}(z=0) \simeq E^{2/3}(z) \cdot R_{200}(z)$, which translates approximately linearly into the total cluster mass $M_{200}(z=0) \simeq E^{2/3}(z) \cdot M_{200}(z) \simeq 1.4 \cdot M_{200}(0.975)$ (see e.g. Equ. 3). However, once including the continuing mass accretion the cluster growth rate since $z \simeq 1$ is much faster. The simulations of Burns et al. (2008) predict average mass growth rates of $\simeq$5-10% per Gyr at late times and $\simeq$30-50% per Gyr during active mass assembly periods around $z \sim 1$. As a benchmark, the time evolution of the largest local $\sim 10^{15}\,M_\odot$ halo in the Millennium-II simulation (Boylan-Kolchin et al. 2009) exhibits a total mass increase since $z \sim 1$ by more than a factor of 5. A realistic prediction for the evolved total cluster mass of XMMU J1230.3+1339 at the current epoch is hence $M_{200}(z=0) \sim (1.5$-$2) \times 10^{15}\,M_\odot$, i.e. ranked among the most massive local clusters and likely even higher in mass compared to the Coma system with $M \simeq 10^{15}\,M_\odot$.

From the X-ray perspective, Coma is a prototype Non-Cool-Core cluster featuring a shallow surface brightness profile with a large core radius of $r_c \sim 300$ kpc (e.g. Briel et al. 1992). A similar X-ray appearance can be expected for XMMU J1230.3+1339, which shows already in the current configuration a very extended NCC SB distribution. The core impact of the BCG2 group and subsequently accreted matter (Sect. 5.1) will likely further disperse the remaining central ICM density peak within the next Gigayear (Figs. 8, 9) resulting in an even more flattened X-ray SB profile for the expected new equilibrium configuration a few Gyr later.

The upcoming merging with the BCG2 group will lead to another close resemblance to Coma in the optical, namely the existence of two central, almost equally massive brightest galaxies. The core impact velocity of the BCG2 group with the main halo is too high (see Sect. 4.4) to allow efficient merging with other central galaxies, i.e. BCG2 is expected to retain its entity as a massive galaxy. After relaxation within the main cluster halo and several Gyr of dynamical friction at work, BCG2 can be expected to settle close to the cluster center at low redshifts and form a pair of two dominant cluster galaxies together with the nominal BCG. In terms of the general optical richness, XMMU J1230.3+1339 is already comparable to Coma (richness class R=2) when considering the accessible bright end of the galaxy population. With the continuing accretion of galaxies from the surrounding filaments, the new system is likely to surpass Coma in optical richness by $z=0$.

Coma is also the prototype for clusters featuring a diffuse radio halo. In Sect. 4.4, we discussed the possibility that such a radio halo originates from merging events such as the one observed in XMMU J1230.3+1339. If this scenario prevails, the evolved cluster might additionally show similarity to Coma in the radio regime at certain epochs.

6. Summary and conclusions

We have presented a multi-wavelength analysis and characterization of the galaxy cluster XMMU J1230.3+1339 at $z=0.975$, which is summarized in the following. An overview of the system parameters and the derived mass estimates is provided in Table 3.

1. The galaxy cluster was discovered within the XMM-*Newton* Distant Cluster Project (XDCP) as a bright, extended X-ray source in an archival XMM-*Newton* observation targeting the Virgo galaxy NGC 4477.
2. We have characterized the X-ray properties of the system with a joint analysis of the XMM-*Newton* data and additional archival *Chandra* observations finding a bolometric luminosity of $L_{X,500}^{bol} \simeq 6.50 \times 10^{44}\,\text{erg s}^{-1}$ ($\pm 10\%$), an ICM temperature of $T_{X,2500} \simeq 5.30$ keV ($\pm 13\%$), a gas mass of $M_{gas,500} \simeq 3.0 \times 10^{13}\,M_\odot$ ($\pm 30\%$), a gas mass fraction of $f_{gas,500} \simeq 0.10$ ($\pm 35\%$) consistent with local values, and a Y_X parameter of $Y_{X,500} \simeq 1.6 \times 10^{14}\,M_\odot$ keV ($\pm 38\%$).
3. The *Chandra* analysis of the X-ray surface brightness distribution yielded an approximate core radius of 215 kpc, a β profile parameter of 0.84, and an overall classification as a Non-Cool-Core cluster. The very central part of the SB profile is better represented by a double β-model with an additional more compact radial component, from which we derive a central electron density of $n_{e,0} \simeq 2.3 \times 10^{-2}\,\text{cm}^{-3}$ ($\pm 60\%$) and a corresponding cooling time of about 4 Gyr.
4. The cluster features a very rich galaxy population (Abell richness R=2, $N_{200} \simeq 57$) with a prominent red-sequence in the color-magnitude-diagram and a total z'-band luminosity of $L_{500,ap}^{tot,z'} \simeq 1.06 \times 10^{13}\,L_\odot$ ($\pm 15\%$).

Table 3. Multi-wavelength properties of the cluster XMMU J1230+1339.

Property	Value	Unit	M_{200}^{est} $[10^{14}\,M_\odot]$
RA	12:30:16.9		
DEC	13:39:04		
N_H	2.62×10^{20}	cm^{-2}	
z	0.975 ± 0.002		
M_{200}^{best}	$4.19^{+0.79}_{-0.77} \times 10^{14}$	$M_\odot$	
$R_{X,200}$	1017^{+68}_{-60}	kpc	
$R_{X,500}$	670^{+45}_{-39}	kpc	
$R_{X,2500}$	297^{+20}_{-17}	kpc	
$T_{X,2500}$	$5.30^{+0.71}_{-0.62}$	keV	$3.61^{+0.77(+0.73)}_{-0.68}$
$T_{X,71''}$	$6.0^{+1.6}_{-1.2}$	keV	
$Z_{X,2500}$	$0.43^{+0.24}_{-0.19}$	$Z_\odot$	
$f_{X,500}^{0.5-2\,keV}$	$(5.14 \pm 0.54) \times 10^{-14}$	$erg\,s^{-1}\,cm^{-2}$	
$L_{X,500}^{0.5-2\,keV}$	$(1.92 \pm 0.20) \times 10^{44}$	$erg\,s^{-1}$	
$L_{X,[0.15-1]500}^{0.5-2\,keV}$	$(1.53 \pm 0.21) \times 10^{44}$	$erg\,s^{-1}$	
$L_{X,500}^{bol}$	$(6.50 \pm 0.68) \times 10^{44}$	$erg\,s^{-1}$	$4.1^{\pm 0.6(\pm 1.0)}$
Z_{2500}	$0.43^{+0.24}_{-0.19}$	$Z_\odot$	
β_X	0.84 ± 0.47		$4.9^{\pm 2.8}$
r_c	215 ± 110	kpc	
c_{SB}	0.07		
$n_{e,0}$	$(2.3 \pm 1.4) \times 10^{-2}$	cm^{-3}	
$t_{cool,20kpc}$	4.0 ± 2.4	Gyr	
c_{sound}	1160	km/s	
$M_{gas,500}$	$(3.0 \pm 0.9) \times 10^{13}$	$M_\odot$	$4.2^{\pm 1.5}$
$Y_{X,500}$	$1.6^{\pm 0.5(+0.2)} \times 10^{14}$	$M_\odot$ keV	$3.6^{\pm 1.1(+0.4)}$
$f_{gas,500}$	0.100 ± 0.035		
R^{rich}	2		
N_{200}	57		$6.3^{\pm 0.7(\pm 2.0)}$
L_{200}^z	$(9.2 \pm 2.3) \times 10^{12}$	$L_\odot$	$11.1^{\pm 2.8(\pm 3.7)}$
$L_{500}^{tot,z}$	$(1.06 \pm 0.16) \times 10^{13}$	$L_\odot$	
$R-z$	2.05 ± 0.10	mag	
m_{BCG}^z	19.90 ± 0.02	mag	
M_{BCG}^z	-24.95 ± 0.03	mag	$4.4^{+0.7(+1.0)}_{-0.7(-2.2)})$
d_{BCG}^{center}	140	kpc	
σ_r	658 ± 277	km/s	$2.8^{+5.2}_{-2.3}$
$M/L^{z'}$	46.7 ± 11.3	$M_\odot/L_\odot$	
opt_{opt}			$8.6^{+1.3(+2.8)}_{-1.3(-3.9)}$
WL σ_r^{SIS}	$1\,271 \pm 275$	km/s	$7.6^{+3.3(+3.0)}_{-3.3}$
WL NFW			$6.9^{+3.3(+2.2)}_{-3.3}$
$P_{1440\,MHz}$	8.3×10^{24}	$W\,Hz^{-1}$	$9.5^{\pm 3.8}$

5. The Brightest Cluster Galaxy is located at a projected distance of 140 kpc from the nominal cluster center and has a luminosity of $L_{BCG}^z \simeq 6.1 \times 10^{11} \, L_\odot$, two magnitudes brighter than the characteristic L_* luminosity at this redshift.

6. Based on 13 secure spectroscopic cluster members, we find a radial velocity dispersion estimate of $\sigma_r \simeq 658 \, \mathrm{km/s} \, (\pm 42\%)$.

7. As presented in detail in the accompanying Paper II of Lerchster et al. (2010), we detect a weak gravitational lensing signal for the cluster on the $3.5 \, \sigma$ significance level, which currently sets the redshift limit for the extraction of a weak lensing signal based on ground imaging.

8. We have performed a multi-wavelength analysis of the cluster structure based on projected density maps of (i) red galaxies, (ii) the X-ray surface brightness, (iii) the total z′-band light, and (iv) the weak lensing mass distribution. We find a well defined concordant cluster center and a main elongation axis along the SE-NW direction present in all maps.

9. Several cluster-associated sub-components were identified on different cluster-centric distance scales ranging from a merging event in the central region to two infalling groups on the cluster outskirts and two galaxy filaments extending beyond the nominal cluster radius.

10. One of the groups has recently entered the R_{500} radius of the cluster along a radial infall orbit. The central dominant galaxy of this group has also BCG properties and is only marginally fainter than the nominal Brightest Cluster Galaxy.

11. We find evidence for a central fly-through group 'bullet' close to cluster core passage from a wedge-like X-ray surface brightness feature, an associated off-center galaxy density and luminosity peak with the front end aligned to the X-ray surface brightness jump, indications for tidally disrupted galaxies, blue-shifted redshifts in the cluster-centric reference frame, and a matching elongation in the weak lensing mass map.

12. Marginally extended 1.4 GHz radio emission located in the wake region of the central merging group along the axis of the apparent 'bullet' trajectory is detected by the VLA FIRST survey. The origin of this radio emission could be associated to an extended radio jet connected to the center of one of the nearby cluster galaxies, or possibly the direct observable result of ultra-relativistic particle acceleration in the turbulent wake region of the merger, as predicted by simulations. A cross-check with the scaling relation for the total power in lower-z radio halos with the observed radio source in the cluster is reasonably consistent with the possibility that they share a related physical origin.

13. We have attempted a tentative reconstruction of the 3D-accretion geometry of the cluster environment that connects the identified associated components with available redshift information to the main halo.

14. We have derived 13 proxies for the total cluster mass from the different wavelength regimes. The combination of four reliable quasi-independent mass estimates yielded a joint best estimate for the total cluster mass of $M_{200}^{best} \simeq 4.19 \times 10^{14} \, M_\odot$ ($\pm 19\%$). All X-ray derived mass estimates are in good agreement with this preferred mass interval, the weak lensing results are consistent within the currently larger statistical uncertainties, and the tested optical mass proxies tend to suggest significantly higher total system masses, albeit with large systematic uncertainties.

15. We argued that the cluster will likely evolve into a Coma-like system with expected similarities in the ICM structure, the optical appearance with two dominant central galaxies, and possibly even surpass Coma in terms of galaxy richness and total mass.

The newly identified galaxy cluster XMMU J1230.3+1339 is an excellent test laboratory at $z \sim 1$ for detailed observational studies to address various fundamental questions related to the assembly phase of massive systems and their Dark Matter, ICM, and galaxy components. Recent follow-up campaigns of the cluster environment include additional optical spectroscopy at VLT/FORS 2, deeper X-ray coverage with *Chandra*, and mm observations with APEX-SZ. Upcoming studies will e.g. aim to derive a more detailed picture on the interaction processes of the different components related to the central merging event or to characterize the galaxy populations as a function of cluster-centric distance in different sub-components and the large-scale structure filaments.

References

Abell, G. O. 1958, ApJS, 3, 211
Allen, S. W., Rapetti, D. A., Schmidt, R. W., et al. 2008, MNRAS, 383, 879
Andreon, S., Valtchanov, I., Jones, L. R., et al. 2005, MNRAS, 359, 1250
Arnaud, M., Pointecouteau, E., & Pratt, G. W. 2005, A&A, 441, 893
Arnaud, M., Pointecouteau, E., & Pratt, G. W. 2007, A&A, 474, L37
Arnaud, M., Pratt, G. W., Piffaretti, R., et al. 2010, A&A, 517, A92
Becker, R. H., Helfand, D. J., White, R. L., Gregg, M. D., & Laurent-Muehleisen, S. A. 2003, VizieR Online Data Catalog, 8071, 0
Beers, T. C., Flynn, K., & Gebhardt, K. 1990, AJ, 100, 32
Bertin, E. 2006, in Astronomical Society of the Pacific Conference Series, Vol. 351, Astronomical Data Analysis Software and Systems XV, ed. C. Gabriel, C. Arviset, D. Ponz, & S. Enrique, 112
Bertin, E. & Arnouts, S. 1996, A&AS, 117, 393
Biviano, A., Murante, G., Borgani, S., et al. 2006, A&A, 456, 23
Blanton, M. R., Hogg, D. W., Bahcall, N. A., et al. 2003, ApJ, 592, 819
Böhringer, H., Mullis, C. R., Rosati, P., et al. 2005, ESO Messenger, 120, 33
Böhringer, H., Schuecker, P., Guzzo, L., et al. 2004, A&A, 425, 367
Böhringer, H., Schuecker, P., Pratt, G. W., et al. 2007, A&A, 469, 363
Böhringer, H., Voges, W., Huchra, J. P., et al. 2000, ApJS, 129, 435
Boylan-Kolchin, M., Springel, V., White, S. D. M., Jenkins, A., & Lemson, G. 2009, MNRAS, 398, 1150
Bradač, M., Clowe, D., Gonzalez, A. H., et al. 2006, ApJ, 652, 937
Bremer, M. N., Valtchanov, I., Willis, J., et al. 2006, MNRAS, 371, 1427
Briel, U. G., Henry, J. P., & Boehringer, H. 1992, A&A, 259, L31
Brunetti, G., Blasi, P., Cassano, R., & Gabici, S. 2004, MNRAS, 350, 1174
Brunetti, G., Cassano, R., Dolag, K., & Setti, G. 2009, A&A, 507, 661
Brunetti, G., Setti, G., Feretti, L., & Giovannini, G. 2001, MNRAS, 320, 365
Bullock, J. S., Kolatt, T. S., Sigad, Y., et al. 2001, MNRAS, 321, 559
Burns, J. O., Hallman, E. J., Gantner, B., Motl, P. M., & Norman, M. L. 2008, ApJ, 675, 1125
Carlberg, R. G., Yee, H. K. C., Ellingson, E., et al. 1997, ApJ, 485, L13
Cassano, R., Brunetti, G., Setti, G., Govoni, F., & Dolag, K. 2007, MNRAS, 378, 1565
Cavaliere, A. & Fusco-Femiano, R. 1976, A&A, 49, 137
Clowe, D., Bradač, M., Gonzalez, A. H., et al. 2006, ApJ, 648, L109
Danese, L., de Zotti, G., & di Tullio, G. 1980, A&A, 82, 322
De Luca, A. & Molendi, S. 2004, A&A, 419, 837

De Lucia, G., Poggianti, B. M., Aragón-Salamanca, A., et al. 2007, MNRAS, 374, 809
Demarco, R., Wilson, G., Muzzin, A., et al. 2010, ApJ, 711, 1185
Dolag, K., Bartelmann, M., Perrotta, F., et al. 2004, A&A, 416, 853
Dolag, K., Bykov, A. M., & Diaferio, A. 2008, Space Science Reviews, 134, 311
Dunn, R. J. H., Allen, S. W., Taylor, G. B., et al. 2010, MNRAS, 404, 180
Eisenhardt, P. R. M., Brodwin, M., Gonzalez, A. H., et al. 2008, ApJ, 684, 905
Erben, T., Schirmer, M., Dietrich, J. P., et al. 2005, Astronomische Nachrichten, 326, 432
Ettori, S., Tozzi, P., Borgani, S., & Rosati, P. 2004, A&A, 417, 13
Fassbender, R. 2007, Phd thesis, Ludwig-Maximilians-Unversität München, astro-ph/0806.0861
Fassbender, R., Böhringer, H., Lamer, G., et al. 2008, A&A, 481, L73
Feretti, L. & Giovannini, G. 2008, in Lecture Notes in Physics, Berlin Springer Verlag, Vol. 740, A Pan-Chromatic View of Clusters of Galaxies and the Large-Scale Structure, ed. M. Plionis, O. López-Cruz, & D. Hughes, 143
Ferrari, C., Govoni, F., Schindler, S., Bykov, A. M., & Rephaeli, Y. 2008, Space Science Reviews, 134, 93
Finn, R. A., Zaritsky, D., McCarthy, Jr., D. W., et al. 2005, ApJ, 630, 206
Finoguenov, A., Guzzo, L., Hasinger, G., et al. 2007, ApJS, 172, 182
Finoguenov, A., Watson, M. G., Tanaka, M., et al. 2010, MNRAS, 258
Fioc, M. & Rocca-Volmerange, B. 1997, in ASSL Vol. 210: The Impact of Large Scale Near-IR Sky Surveys, 257
Fujita, Y., Takizawa, M., & Sarazin, C. L. 2003, ApJ, 584, 190
Girardi, M., Biviano, A., Giuricin, G., Mardirossian, F., & Mezzetti, M. 1993, ApJ, 404, 38
Gladders, M. D. & Yee, H. K. C. 2005, ApJS, 157, 1
Guzzo, L., Pierleoni, M., Meneux, B., et al. 2008, Nature, 451, 541
Hicks, A. K., Ellingson, E., Bautz, M., et al. 2008, ApJ, 680, 1022
Huang, X., Morokuma, T., Fakhouri, H. K., et al. 2009, ApJ, 707, L12
Jee, M. J., Rosati, P., Ford, H. C., et al. 2009, ApJ, 704, 672
Jee, M. J., White, R. L., Ford, H. C., et al. 2005, ApJ, 634, 813
Jee, M. J., White, R. L., Ford, H. C., et al. 2006, ApJ, 642, 720
Kodama, T. & Arimoto, N. 1997, A&A, 320, 41
Koester, B. P., McKay, T. A., Annis, J., et al. 2007a, ApJ, 660, 239
Koester, B. P., McKay, T. A., Annis, J., et al. 2007b, ApJ, 660, 221
Kotov, O. & Vikhlinin, A. 2005, ApJ, 633, 781
Kravtsov, A. V., Vikhlinin, A., & Nagai, D. 2006, ApJ, 650, 128
Kurk, J., Cimatti, A., Zamorani, G., et al. 2009, A&A, 504, 331
Kurtz, M. J. & Mink, D. J. 1998, PASP, 110, 934
Laing, R. A. & Peacock, J. A. 1980, MNRAS, 190, 903
Leauthaud, A., Finoguenov, A., Kneib, J., et al. 2010, ApJ, 709, 97
Lerchster, M., Seitz, S., Brimioulle, F., & et al. 2010, MNRAS, submitted [`www.usm.uni-muenchen.de/people/mike/XMMUJ1230_MNRAS.pdf`]
Lin, Y.-T. & Mohr, J. J. 2004, ApJ, 617, 879
Lumb, D. H., Warwick, R. S., Page, M., & De Luca, A. 2002, A&A, 389, 93
Markevitch, M., Gonzalez, A. H., David, L., et al. 2002, ApJ, 567, L27
Markevitch, M. & Vikhlinin, A. 2007, Phys. Rep., 443, 1
Marrone, D. P., Smith, G. P., Richard, J., et al. 2009, ApJ, 701, L114
Maughan, B. J., Jones, L. R., Ebeling, H., & Scharf, C. 2006, MNRAS, 365, 509
Mei, S., Holden, B. P., Blakeslee, J. P., et al. 2009, ApJ, 690, 42
Meneghetti, M., Rasia, E., Merten, J., et al. 2010, A&A, 514, A93+
Mullis, C. R., Rosati, P., Lamer, G., et al. 2005, ApJ, 623, L85
Muzzin, A., Wilson, G., Yee, H. K. C., et al. 2009, ApJ, 698, 1934
Nagai, D., Kravtsov, A. V., & Vikhlinin, A. 2007, ApJ, 668, 1
Navarro, J. F., Frenk, C. S., & White, S. D. M. 1997, ApJ, 490, 493
O'Hara, T. B., Mohr, J. J., & Sanderson, A. J. R. 2007, arXiv:0710.5782
Perlman, E. S., Horner, D. J., Jones, L. R., et al. 2002, ApJS, 140, 265
Pierre, M., Pacaud, F., Duc, P.-A., et al. 2006, MNRAS, 372, 591
Pivato, M. C., Padilla, N. D., & Lambas, D. G. 2006, MNRAS, 373, 1409
Popesso, P., Biviano, A., Böhringer, H., & Romaniello, M. 2007, A&A, 464, 451
Popesso, P., Biviano, A., Böhringer, H., Romaniello, M., & Voges, W. 2005, A&A, 433, 431
Pratt, G. W., Arnaud, M., Piffaretti, R., et al. 2010, A&A, 511, A85
Pratt, G. W., Croston, J. H., Arnaud, M., & Böhringer, H. 2009, A&A, 498, 361
Reiprich, T. H. & Böhringer, H. 2002, ApJ, 567, 716
Reyes, R., Mandelbaum, R., Hirata, C., Bahcall, N., & Seljak, U. 2008, MNRAS, 390, 1157
Rosati, P., Borgani, S., & Norman, C. 2002, ARA&A, 40, 539
Rosati, P., Tozzi, P., Gobat, R., et al. 2009, A&A, 508, 583
Rovilos, E., Burwitz, V., Szokoly, G., et al. 2009, A&A, 507, 195
Sanderson, A. J. R., Edge, A. C., & Smith, G. P. 2009, MNRAS, 398, 1698
Santos, J. S., Rosati, P., Gobat, R., et al. 2009, A&A, 501, 49
Santos, J. S., Rosati, P., Tozzi, P., et al. 2008, A&A, 483, 35
Sarazin, C. L. 1986, Reviews of Modern Physics, 58, 1
Scharf, C. 2002, ApJ, 572, 157
Schwope, A. D., Lamer, G., de Hoon, A., et al. 2010, A&A, 513, L10
Shibata, R., Matsushita, K., Yamasaki, N. Y., et al. 2001, ApJ, 549, 228
Springel, V. & Farrar, G. R. 2007, MNRAS, 380, 911
Stanek, R., Rasia, E., Evrard, A. E., Pearce, F., & Gazzola, L. 2010, ApJ, 715, 1508
Stanford, S. A., Eisenhardt, P. R., Brodwin, M., et al. 2005, ApJ, 634, L129
Stanford, S. A., Romer, A. K., Sabirli, K., et al. 2006, ApJ, 646, L13
Staniszewski, Z., Ade, P. A. R., Aird, K. A., et al. 2009, ApJ, 701, 32
Takizawa, M. 2005, ApJ, 629, 791
Tanaka, M., Finoguenov, A., & Ueda, Y. 2010, ApJ, 716, L152
Tanaka, M., Kodama, T., Kajisawa, M., et al. 2007, MNRAS, 377, 1206
Tozzi, P., Rosati, P., Ettori, S., et al. 2003, ApJ, 593, 705
van Breukelen, C., Clewley, L., Bonfield, D. G., et al. 2006, MNRAS, 373, L26
Vanderlinde, K., Crawford, T. M., de Haan, T., et al. 2010, arXiv:1003.0003
Vazza, F., Brunetti, G., Kritsuk, A., et al. 2009, A&A, 504, 33
Vikhlinin, A., Burenin, R. A., Ebeling, H., et al. 2009a, ApJ, 692, 1033
Vikhlinin, A., Kravtsov, A. V., Burenin, R. A., et al. 2009b, ApJ, 692, 1060
Vikhlinin, A., VanSpeybroeck, L., Markevitch, M., Forman, W. R., & Grego, L. 2002, ApJ, 578, L107
Voit, G. M. 2005, Advances in Space Research, 36, 701
White, R. L., Becker, R. H., Helfand, D. J., & Gregg, M. D. 1997, ApJ, 475, 479
Wilson, G., Muzzin, A., Yee, H. K. C., et al. 2009, ApJ, 698, 1943
Zhang, Y., Finoguenov, A., Böhringer, H., et al. 2008, A&A, 482, 451
Zibetti, S., White, S. D. M., Schneider, D. P., & Brinkmann, J. 2005, MNRAS, 358, 949